Angular-based modeling of unbalanced magnetic pull for analyzing the dynamical behavior of a 3-phase induction motor

Xiaowen Li, Adeline Bourdon, Didier Rémond, Samuel Kœchlin, Dany Prieto

To cite this version:

Xiaowen Li, Adeline Bourdon, Didier Rémond, Samuel Kœchlin, Dany Prieto. Angular-based modeling of unbalanced magnetic pull for analyzing the dynamical behavior of a 3-phase induction motor. Journal of Sound and Vibration, 2021, 494, pp.115884 -. 10.1016/j.jsv.2020.115884 . hal-03493567

HAL Id: hal-03493567

https://hal.science/hal-03493567v1

Submitted on 15 Dec 2022

Angular-based modeling of unbalanced magnetic pull for analyzing the dynamical behavior of a 3-phase induction motor

Xiaowen Li[a,b,*], Adeline Bourdon[a], Didier Remond[a], Samuel Koechlin[b], Dany Prieto[b]

[a] *Univ Lyon, INSA-Lyon, CNRS UMR5259, LaMCoS, F-69621, Villeurbanne, France*
[b] *NIDEC PSA emotors, 212, Bd Pelletier - 78 955 Carrieres-Sous-Poissy*

Abstract

A multiphysics asynchronous electric machine model based on the angular approach is developed in this paper by adding the interaction between the Unbalanced Magnetic Pull and the rotor center radial displacements to reinforce the electro-magneto-mechanic fields couplings. The novelty of the proposed model lies also in calculating the instantaneous angular speed of the shaft and therefore tackling problems in non-stationary operating conditions. This radial force is generated from the magnetic field distortion mainly due to the rotor eccentricity. The shifted rotor geometric center coordinates are introduced to calculate the effective air gap length in the case with eccentricity. The Permeance Network Method is adopted to describe the magnetic field distribution and the electromagnetic force are achieved by applying the virtual work method. This multiphysics model is validated in the quasi-static regime by comparing with the reference data from the traditional numerical model in the case with and without input eccentricity. The physical characteristics about Unbalanced Magnetic Pull and its frequency components are investigated in angular domain to interpret the transfer path from different angularly-periodic variation fields in the induction machine. The impact of the rotor eccentricity amplitude variation on the dynamic behavior of the electric machine are analyzed at different operating points.

Keywords: Unbalanced Magnetic Pull, Induction motors, Eccentric rotor, Multiphysics model, Angular approach, Electro-magneto-mechanic interaction

---

1. Introduction

Unbalanced Magnetic Pull (UMP) is a phenomenon which often appears in electrical rotating machinery. In the general case, most of electromagnetic energy is converted into mechanical work from the air-gap between the stator and the rotor in the form of the electromagnetic torque and meanwhile the magnetic field also produces some force components along the periphery of this area. With the uniform air-gap, these forces offset each other. However in reality, air-gap is hardly uniform due to either mechanical problems like air-gap eccentricity or unevenness of the electromagnetic field [1]. The latter part is usually caused by some defects in the electromagnetic field which are possible to be detected and avoided but the former term is difficult to avoid for the high precision requirements during the manufacturing and installation processes. In this case, those magnetic force components reveal as a resultant radial force in the motor which is also called as UMP. Once it is produced, this kind of radial force will pull the rotor roughly in the direction of the minimum air-gap and cause some significant effects to the structure like vibration and mechanical wear.

The most difficult part about calculating the UMP is to describe the distorted magnetic field along the

---

[*] Corresponding author
Email address: `xiaowen.li@insa-lyon.fr` (Xiaowen Li)

periphery of the air-gap with rotor eccentricity. There are generally two kinds of traditional methods often adopted in the literature. One is the numerical method also known as finite element method (FEM) which is used widely for its excellent adaptability in all machine types and the high precision of its simulation results. Arkkio et al. [2] used the Time-stepping finite-element analysis to solve the magnetic field when the rotor is in whirling motion and this model is adopted by Holopainen et al. [3–5] to combine with a simple mechanical model in order to study the influence of UMP on the rotor vibration behavior. The same method is also reproduced in Ansys by Donat et al. [6, 7] to realize its application in a commercial software. Meanwhile the analytical method also attracts some attention from the researchers for its small calculating efforts and the simple way to analyze the variation of the global value. Different models are established in the frame of analytical method. One popular of them is the air-gap permeance approach. It is firstly proposed by Belmans et al. [8]. They expressed the air-gap magnetic flux density distribution as the product of the magneto-motive force (MMF) and the air-gap permeance. In order to simplify the calculation, air-gap permeance is expanded as Fourier series by conserving only the first-harmonic component. This method is adopted by Smith et al. [9], Guo et al. [10] and Gerlando et al. [11] to calculate the UMP generated by a relatively small eccentricity with the assumption of the spatial linearity of the air gap flux density distribution. The traditional numerical method consumes too much time during the dynamic simulation and the classic analytical method lacks the close bond with the local geometry of the electrical machine. Therefore in this paper, in order to simulate the extreme case with a relatively large eccentricity, Permeance Network Method (PNM) belonging to one of the magnetic equivalent circuit (MEC) model is adopted to describe the whole magnetic field. It is essentially a numerical method but it can be regarded as a compromise between the electrical lumped-parameter models and the finite element analysis. PNM is firstly introduced in the book of Ostovic [12] systematically and adopted by Mahyob et al. [13] for the diagnosis of stator faults in the electrical machines and developed by Han et al. [14] to study the unstable forces due to the induction motor eccentricity.

The UMP analysis realized in some literatures can't be considered as a complete analysis because of their weak coupling with the mechanical part. Some of them like Arkkio et al. [2], Smith et al. [9], Kelk et al. [15] and Gerlando et al. [11], just calculate the UMP with a set-up rotor eccentricity and study its influence on the rotor dynamic behavior but there is no reaction from the mechanical part to the electromagnetic field. Some others introduced the mechanical part by a simple mechanical rotational motion equation as [16] without the consideration about the radial movement. Afterwards people begin to realize the importance of the strong coupling with the mechanic field for analyzing the dynamic behavior of the motor hence some more accurate models to describe the mechanical part appeared. One of the most popular is "Jeffcott-Laval rotor model". By combining the traditional rotor dynamic theory, many motor shaft stability analysis are realized in different kinds of electric machines. Among them, UMP is either treated as an external force generated from the magnetic field to be exerted on the rotor-bearing system [10] or represented by an equivalent negative stiffness in the dynamic differential equation [8, 14]. However since only two degrees of freedom (DOF) are considered in these models, their rotor dynamic simulations have to be performed under the unbalance excitation with a constant rotation speed. And the influence of the radial eccentricity to the rotational movement can't be analyzed even if the distorted magnetic field may also change the generated instant electromagnetic torque value and produce the rotational vibration. As mentioned before most models are established based on the assumption of a constant rotation speed but in reality it can never be reached even in the steady state and on the other hand from the fluctuation of the rotation speed, the variation of the generated electromagnetic forces can be detected.

Therefore in this paper the motor shaft is described with several beam elements based on Timoshenko beam theory and the electromagnetic forces (UMP and electromagnetic torque) are calculated and analyzed in the frame of the angular approach in order to take the real fluctuation of the rotation speed into account (more details are given in Section 2.1). This implies a strong coupling between the electro-magneto-mechanic fields and interprets the transfer path from different angularly-periodic variation field in an induction machine.

Fourati et al. [17] have presented a simple asynchronous electrical machine model to describe this multi-physics interaction. Unfortunately, in this previous work the strong coupling with the mechanical part is only realized on the rotational movement to identify the bearing defects represented by the angularly varying resistant torque in the model. In order to reinforce this strong coupling and create a more robust model, the relation between the UMP and the rotor radial displacements is set up in the ancient model and several modifications are applied. The whole system is reorganized in Section 2. The distortion of the magnetic field in the air gap is described by the local air gap permeance values associated with the effective air-gap length due to rotor eccentricities. Therefore in Section 3, the effective air-gap length around the circumstance of the air gap is expressed as the function of the rotor geometric center coordinates and the value of electromagnetic forces are deduced by the principle of virtual work method. From Section 4, this proposed model is firstly validated in the quasi-static regime by comparing with the reference data from the numerical model in the case with and without eccentricity. And then the physical and frequency characteristics about UMP are investigated from the simulation with the input eccentricity about 10% of the average air-gap length (its value is available from Table D.2 in Appendix D). The rotor eccentricity impacts at different operating points are analyzed by realizing simulations in non-stationary operating conditions. The influence of the eccentricity amplitude variations are studied by comparing their results from the simulations with three different input eccentricity values at the rated state. Finally all the rotor eccentricity effects on the dynamic behavior of the motor system are concluded in Section 5.

2. Model formulation and preliminaries

In order to prepare for inserting the new coupling of UMP in this multiphysics model, a brief introduction about the angular approach and the general presentation of three fields modelings and their combinations are provided in this section.

2.1. Angular approach

Angular approach is a modeling method often used in the rotating machine [18]. The DOF of the rotation angle θ which can be achieved directly from the state vector of the model is chosen as a reference variable to provide the relation between resonant phenomena and cyclic excitations. With the angular approach, the relation between the rotation angle and the time described by the Instantaneous Angular Speed (IAS) function is not imposed but generated by the behavior of the rotating shaft in the modeling. Since the value of the rotation speed is the derivative of the rotation angle, its real variation like the fluctuation due to the cyclic phenomena can be detected from the simulation. In order to maintain the bijective relation between the rotation angle and the time, the rotation speed only needs to be always positive and in the same direction of the electromagnetic torque during the simulation of the motor operation mode. Since the assumption of the constant rotation speed is unnecessary in angular approach, simulations in non-stationary operating conditions can be performed directly without any further assumptions.

2.2. Mechanical modeling

The mechanical part is consisted of the shaft and the support shown in Fig. 1. The rotating shaft is divided into five nodes based on the classical Timoshenko model while the quasi-2D induction motor model is situated on the middle node. The shaft is supported by two bearings which are simplified as two orthogonal springs along x and y directions with two identical stiffness values for each in the present simulation. Their values are available from Table D.2 in Appendix D. The vibration differential equation is applied to interpret the dynamic motion of the system as described in Eq. (1).

$$\mathbf{M} \cdot \ddot{\mathbf{X}} + \mathbf{C} \cdot \dot{\mathbf{X}} + \mathbf{K} \cdot \mathbf{X} = \mathbf{F_{ext}}(t) + \mathbf{F_{mag}}(\mathbf{X}, \mathbf{I}) \tag{1}$$

where $\mathbf{M}$, $\mathbf{C}$ and $\mathbf{K}$ are the matrices of mass, damping and stiffness respectively. $\mathbf{F_{ext}}(t)$ is the vector of the global external forces exerted on the mechanical structure and variated as a function of the time like the load torque T_r shown in Fig. 1, while $\mathbf{F_{mag}}(\mathbf{X}, \mathbf{I})$ are the general magnetic forces generated inside of the motor as the function of the rotor center displacement $\mathbf{X}$ and the electrical currents $\mathbf{I}$. The model in [17] includes only the interaction between the electromagnetic torque T_{em} and the shaft rotation angle θ but in the present model the relation between the electromagnetic radial forces F_{emr} which are also known as UMP and the rotor center radial displacements x_r and y_r will be added to predict the behavior with the rotor eccentricity. The mass and the stiffness matrices $\mathbf{M}$, $\mathbf{K}$ are associated with each structural element of the shaft and the support part by employing their characteristic parameters from Table D.2. Since the stator part of the motor is fixed to the base, only the rotor is taken into account in the modeling with its mass and moment of inertia listed also in Table D.2. Therefore the stator part is considered to be rigid and not to vibrate in this work. As it is mentioned in [17], the structural damping is calculated by adopting the modal damping approach while the damping of the rotational rigid mode is added as a damping elementary matrix. According to this differential equation, the lowest natural frequency of the mechanical part is calculated as 292 Hz. Each node has 6 DOFs to illustrate their displacements in all directions of the space. For example about the k_{th} node in the shaft, their 6 DOFs are shown as $\mathbf{X}_k = \{x, y, z, \theta_x, \theta_y, \theta_z\}_k^t$. From Fig. 1, it can be seen that the displacements of rotor center θ and x_r, y_r are represented by the DOFs of the middle node in the shaft. By transforming it into a state-space form in Eq. (2), one obtains

$$\frac{\mathrm{d}\mathbf{Q_M}}{\mathrm{d}t} = \mathbf{A_M} \cdot \mathbf{Q_M} + \mathbf{B_M} \cdot \mathbf{U}(\mathbf{Q_M}) \tag{2}$$

with the state vector $\mathbf{Q_M} = \{\mathbf{X}, \dot{\mathbf{X}}\}^t$ to display the displacements and velocities of each node about all 6 DOFs at every iteration step. The force term $\mathbf{U}(\mathbf{Q_M})$ is composed of the external applied forces $\mathbf{F_{ext}}(t)$ and the inside generated motor forces $\mathbf{F_{mag}}(\mathbf{X}, \mathbf{I})$.

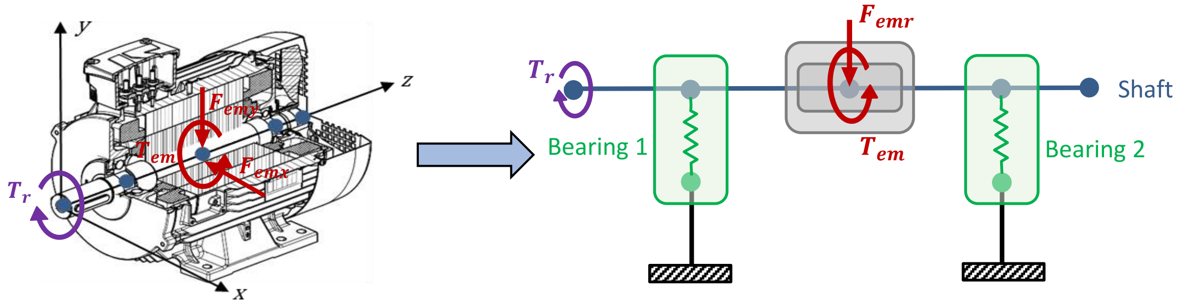

Fig. 1. Mechanical modeling (Bearing stiffness only presented in one direction)

2.3. Magnetic modeling

In order to create a more detailed analytic model, the PNM [12] is adopted to describe the magnetic field in this paper. The motor section (the left schema in Fig. 2) is discretized by a network with various permeance elements ($\mathbf{P_{sy}}, \mathbf{P_{st}}, \mathbf{P_{sl}}, \mathbf{P_{ag}}, \mathbf{P_{rl}}, \mathbf{P_{rt}}, \mathbf{P_{ry}}$) in each branch with the subscripts indicating the respective belonging areas which are shown in different colors in the right schema of Fig. 2. The corresponding magnetic flux ($\boldsymbol{\phi_{sy}}, \boldsymbol{\phi_{st}}, \boldsymbol{\phi_{sl}}, \boldsymbol{\phi_{ag}}, \boldsymbol{\phi_{rl}}, \boldsymbol{\phi_{rt}}, \boldsymbol{\phi_{ry}}$) can only pass through the decided path in a defined direction. The induced MMF sources ($\boldsymbol{\mathcal{F}_{st}}$ and $\boldsymbol{\mathcal{F}_{rt}}$) are set up on the stator and the rotor tooth area respectively. Since the saturation of the magnetic circuit is neglected in this work, the permeance values in the stator and rotor part ($\mathbf{P_{sy}}, \mathbf{P_{st}}, \mathbf{P_{sl}}, \mathbf{P_{rl}}, \mathbf{P_{rt}}, \mathbf{P_{ry}}$) are considered to be constant and are decided by the dimensions of each basic branch element. However the air-gap permeances ($\mathbf{P_{ag}}$) vary as a function of the shaft rotation angle θ and they are also related to the displacements of the rotor center (x_r, y_r) due to the rotor eccentricity in the proposed model. Since the skew of the rotor bars and the steel lamination stack length are considered in calculating the permeance values, this magnetic model is considered as $2.5D$ in this paper. By applying Kirchhoff's current law and Ampere's law, it's easy to deduce the relation between the magnetic flux $\boldsymbol{\phi}$ and the electrical current $\mathbf{I}$ which indicates the coupling of the magneto-electric fields. That leads to Eq. (3).

$$\boldsymbol{\phi} = \mathbf{Gg} \cdot \mathbf{XX(X)} \cdot \mathbf{F_{md}} = \mathbf{Gg} \cdot \mathbf{XX(X)} \cdot \mathbf{ZZ} \cdot \mathbf{I} \tag{3}$$

where $\boldsymbol{\phi}$ is the magnetic flux of each phase, $\mathbf{I}$ is the electrical phase currents, $\mathbf{Gg}$ is a constant matrix that transform the magnetic flux from each branch of the permeance network to those of each phase, $\mathbf{XX(X)}$ is a permeance matrix in function of the rotor center displacements $\mathbf{X}$ (precisely referred to θ, x_r, y_r) which implies the coupling between the mechanical field and the magnetic field, $\mathbf{F_{md}}$ is a vector of MMF and $\mathbf{ZZ}$ is a winding matrix defined by different kinds of windings. The details about the construction of each matrix can be found in [17]. Parameters in the electromagnetic part are calculated automatically according to the motor's geometric dimensions in order to obtain a more closer bond between the motor's behavior and its design.

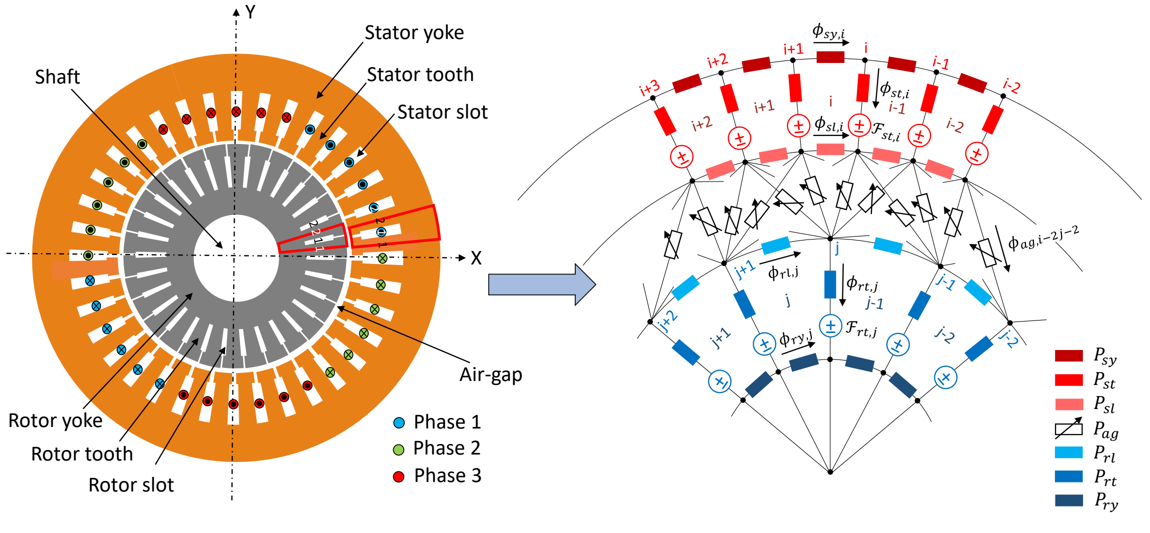

Fig. 2. Magnetic modeling

2.4. Electrical modeling

The electrical model consists of two parts as shown in Fig. 3. One is the three phase windings in the stator and another is the N_r short circuits formed by the squirrel cage in the rotor. The stator windings in Fig. 3a is powered by three phase star connection voltages (V_{12}, V_{23}, V_{31}) which can be replaced by the delta connection in future works. Each phase circuit is simplified by a phase resistance R_{sp} and an electromotive force (EMF) F^e_{sp}. Since the stator windings adopted in this model are the distributed windings connected in series, R_{sp} is the sum of the coil resistance R_{s} from each stator slot in the same phase. The short circuits in the rotor squirrel cage from Fig. 3b are each composed of two ring segments and two adjacent rotor bars. Similar as the stator part, each branch is represented by a resistance R_b or R_r and an EMF F^e_r except for the ring part of the rotor cage because this part isn't involved in producing the EMFs. Different from [17], the rotor bar currents i_b are chosen to be the state vectors instead of the rotor ring currents i_r for the surveillance of the rotor bar fault. Their dynamic behavior is described in Eq. (4).

$$\mathbf{R} \cdot \mathbf{I} + \frac{\mathrm{d}\phi}{\mathrm{d}t} = \mathbf{V}(t) \tag{4}$$

where $\mathbf{R}$ is a matrix of resistance, $\mathbf{I}$ is the state vector containing 3 stator phase currents $\mathbf{i_{sp}}$ and N_r rotor bar currents $\mathbf{i_b}$, $\boldsymbol{\phi}$ is a vector of phase magnetic flux and $\mathbf{V}(t)$ is the supply voltage of three phases which variates as a time function. The Faraday law is applied to realize the connection between the magnetic field and the electric field: $E = \triangle F^e = -\frac{\mathrm{d}\phi}{\mathrm{d}t}$. Like [14], the leakage inductance is ignored since it is small compared to the mutual inductance.

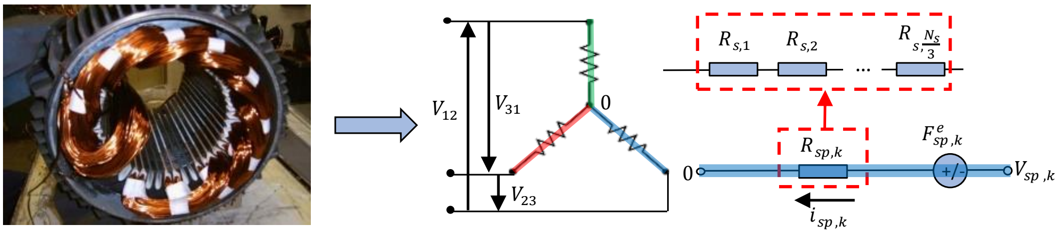

(a) Stator

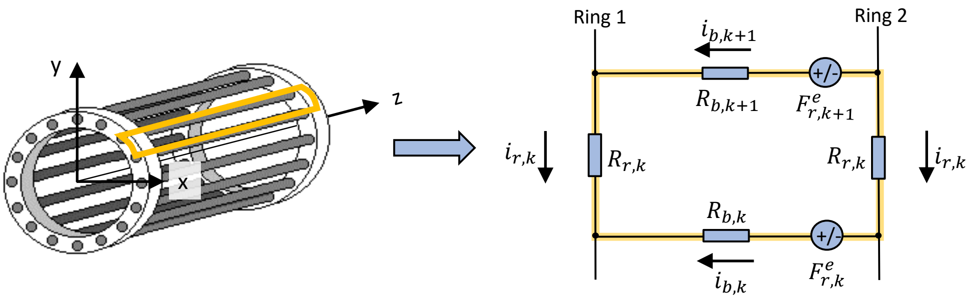

(b) Rotor

Fig. 3. Electrical modeling

2.5. Multiphysics couplings

The multiphysics couplings are realized by solving the global differential equations with a set of global state vectors including mechanical parts (displacements $\mathbf{X}$ and velocities $\dot{\mathbf{X}}$ of all 6 DOFs for each node) and electrical parts (3 stator phase currents and N_r rotor bar currents $\mathbf{I}$). Different from other multiphysics models, this one is considered as a strong coupling which means there is a mutual influence between each of the two fields. Magnetic field and Electrical circuit form the Induction Machine model while the mechanical model is represented by Shaft and Support. Inside of the Induction Machine model, as defined in Eq. (3) and Eq. (4), the stator and rotor phase currents $\mathbf{I}$ are used to calculate the magnetic flux ϕ and meanwhile combined with the supply voltage $\mathbf{V}(t)$ and the instantaneous rotor center velocity ($\dot{\theta}$ and $(\dot{x_r}, \dot{y_r})$), the Faraday law is applied to calculate the electrical phase currents at each moment.

Beside of normal inputs and outputs for each subsystem, one of the outputs from the electromagnetic part "Magnetic forces" (T_{em} and $F_{\text{emx}}, F_{\text{emy}}$) are exerted on the mechanical part to change its dynamic behavior and at the same time these mechanical state values (θ and (x_r, y_r)) variations will react on the electromagnetic part to alter the magnetic field distribution so as to influence their output values like currents and magnetic forces. Thanks to the global state vector, this mutual influence energy conversion happens simultaneously and automatically in this model which is able to describe the real dynamic behavior of electrical machines. This multiphysics model considering about the rotor eccentricities is illustrated in Fig. 4. Those input rotor eccentricity parameters ((x_s, y_s), δ_0 and γ) are explained later in Section 3.

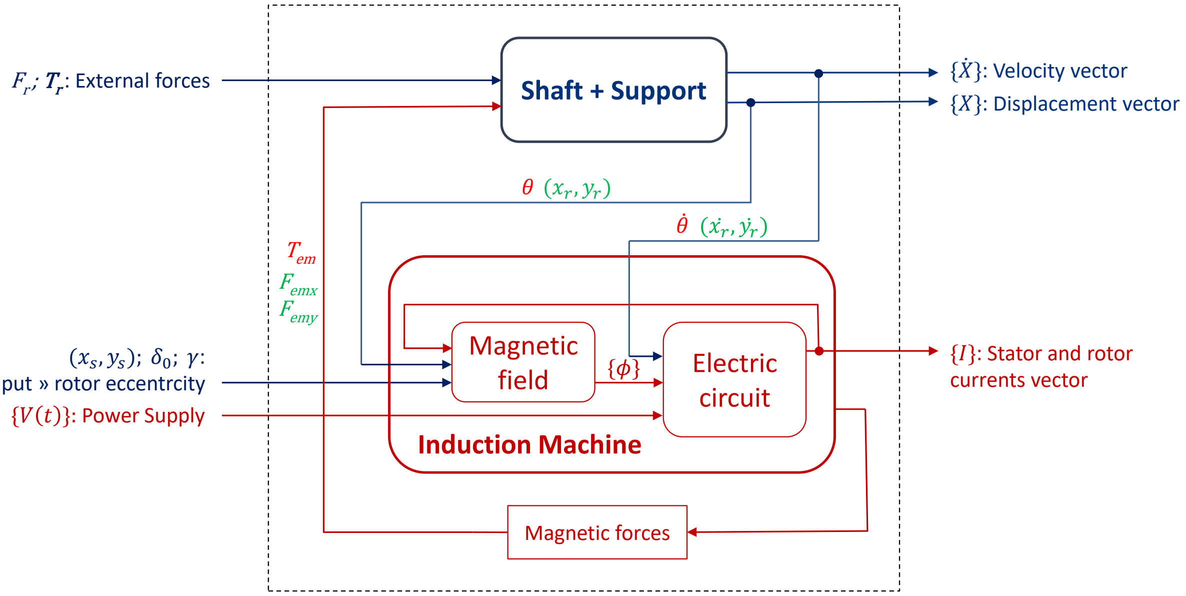

Fig. 4. Multiphysics couplings

3. Unbalanced Magnetic Pull on an eccentric rotor

When talking about the eccentricity in electrical machines, three types of rotor eccentricities are usually defined and studied respectively: static eccentricity [16], dynamic eccentricity [19, 20] and the mix of the two [9, 10, 21]. Those three eccentricity types tend to coexist in reality, especially in our multiphysics model. Since the mechanical coupling is taken into account, all of three types of air-gap eccentricities mentioned before are reduced to mixed one. Owing to our multiphysics model, the rotor geometric center isn't fixed but varies with every shaft revolution. Thus even if a defined static eccentricity is imported into the system, a dynamic movement of the rotor center position will be generated in the model during the simulation. Therefore it's necessary to calculate the UMP with a general formulation based on the actual position of the rotor geometric center which can be used to introduce every kinds of input eccentricities automatically. More details are available in Appendix A.

3.1. Calculation of the effective air-gap length

According to the permeance network in Fig. 2, the air-gap permeances are described as the sum of the permeances between each pair of stator (i) and rotor (j) tooth at each moment where i and j are the integers referred to $i \subseteq [1, N_s]$ and $j \subseteq [1, N_r]$ with N_s, N_r denote to the stator and rotor teeth number respectively. As mentioned previously in the Magnetic modeling (Section 2.3), their values are considered to be parametrically nonlinear and are described as a formula in the function of the rotor geometric center coordinate and the shaft rotation angle:

$$P_{ij}(x_G, y_G, \theta_{ij}) = \frac{P_{\text{maxc}}}{e_i(x_G, y_G)} \cdot f_p(\theta_{ij}) \tag{5}$$

where x_G, y_G are the coordinates of rotor geometric center, θ_{ij} is the relative angle between arbitrary stator tooth i and rotor tooth j which is described in Eq. (6) .

$$\theta_{ij} = \theta_{\text{rt},j} + \theta - \theta_{\text{st},i} \tag{6}$$

where $\theta_{\text{rt},j}$ is the angular position of rotor tooth j, $\theta_{\text{st},i}$ is the angular position of stator tooth i and θ is the shaft rotation angle at each moment.

Eq. (5) defines the air-gap permeances between each pair of stator and rotor tooth in the case of rotor eccentricity and its three components are explained in the following part.

1. P_{maxc} describes the maximum permeance value between one pair of rotor and stator teeth taking the rotor bars skewing angle into account as shown in Eq. (B.1) from Appendix B.

2. $f_p(\theta_{ij})$ represents the air-gap permeance scale factor variation between one pair of stator and rotor teeth as shown in Fig. 5. It is defined in Eq. (C.1) from Appendix C based on the Ostovic model [12]. And then it is developed to the adjacent pair of teeth around the periphery of the air-gap as shown in Fig. 6 where $\tilde{\theta_{ij}}$ is the abscissa to describe the relative angular position between two pairs of stator and rotor teeth. It can be seen that in the case with eccentricity, the family of the permeances according to i_{th} stator tooth have the same amplitude like $\max(P_{i,j}) = \max(P_{i,j-1})$ but the amplitudes of the permeances according to another stator tooth will vary as $\max(P_{i,j}) \neq \max(P_{i+1,j})$ due to the variation of the effective air-gap length. Here, we assumed that only the amplitude will change when we move to the next stator tooth but there is no change on the variation form of $f_p(\theta_{ij})$.

3. $e_i(x_G, y_G)$ is the effective air-gap length according to each stator tooth position in consideration of the rotor eccentricity.

The former two terms can be considered as two constant parts because they are decided once the geometry of the reference machine is defined. Consequently the description of the effective air-gap length in the function of the rotor geometric center coordinates is very important to calculate the air-gap permeances.

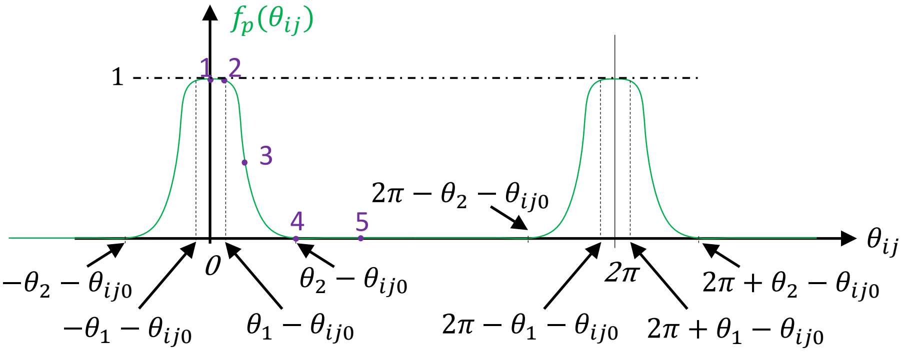

Fig. 5. The shape function of the air-gap permeance between any two opposite teeth versus their relative angle position

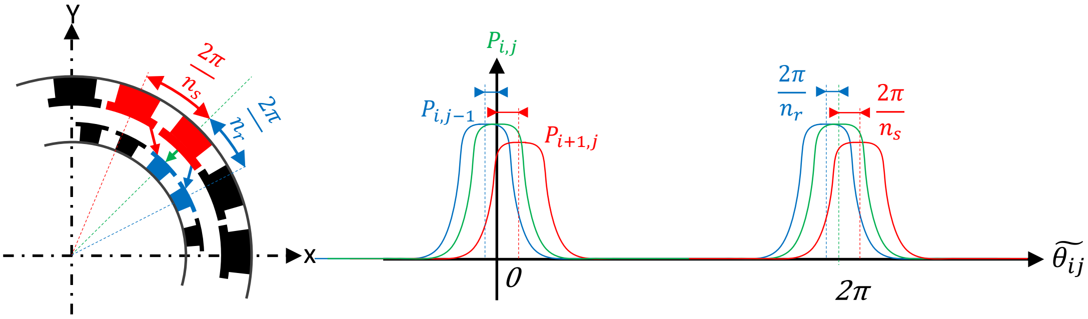

Fig. 6. Evolution of air-gap permeance of adjacent teeth

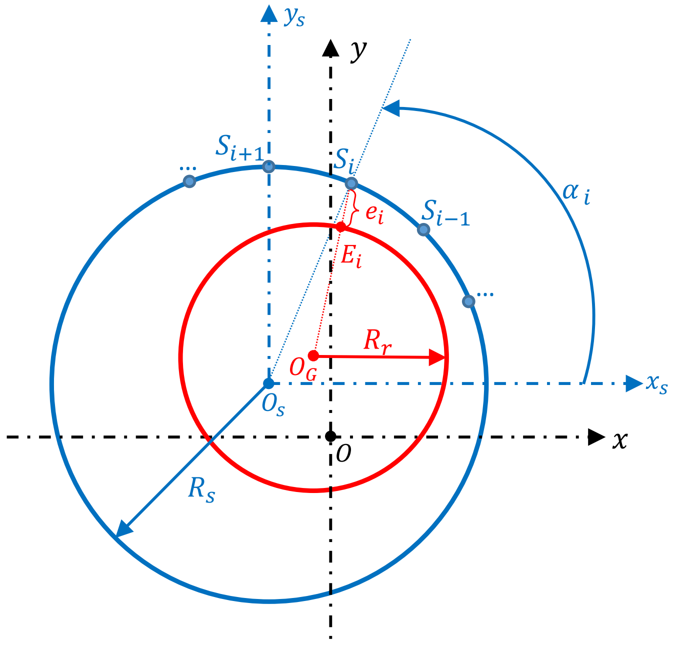

Fig. 7. Calculation of the instantaneous air-gap length e_i associated with the stator tooth i

Fig. 7 shows the distribution of the effective air-gap length around the periphery of the stator inner ring (blue circle) and the rotor outer ring (red circle) with respect to each stator tooth position (blue nodes evenly distributed on the blue circle) at a certain moment. O_G is the rotor geometric center whose position is defined as the function of the rotor center displacements (x_r, y_r) (more details are available in Appendix A) and O_S is the stator center which is introduced to describe the input static eccentricity generated by the parallel misalignment of the rotor and stator center axis due to the installation deviation. Two different radius R_r and R_s are denoted to the rotor outer ring and the stator inner ring respectively. E_i is the interaction point of the line $O_G S_i$ and the rotor outer ring. Every stator tooth position $\theta_{st,i}$ from Eq. (6) is expressed in Fig. 7 by its angular position α_i around the stator inner ring which is defined as:

$$\alpha_i = \frac{2\pi}{N_s} * (i - 1) \tag{7}$$

where i is the integer belonged to $[1, N_s]$.

The effective air-gap length e_i is defined as the minimum distance between this stator tooth and the rotor outer ring. According to each stator tooth position point S_i, the instantaneous effective air-gap length is deduced as

$$e_i = \| E_i S_i \| = \| O_G S_i \| - R_r \tag{8}$$

Two sets of coordinate systems are defined in Fig. 7, one is the $x_s - y_s$ with the origin of the stator center O_S and another is the reference coordinate xOy that is established by taking the initial position of the rotor center as the origin point O. They are parallel to each other. In the coordinate $x_s O_S y_s$, the vector $\mathbf{O_S S_i}$ is defined as $(R_s \cos\alpha_i,\ R_s \sin\alpha_i)$. In the fundamental orthogonal coordinate system xOy, the coordinates of O_G and O_S are identified as (x_G, y_G) and (x_s, y_s) separately. So the vector $\mathbf{O_G S_i}$ appears as:

$$\mathbf{O_G S_i} = \mathbf{O_G O_S} + \mathbf{O_S S_i} = (x_s - x_G, y_s - y_G) + (R_s \cos\alpha_i, R_s \sin\alpha_i) = (R_s \cos\alpha_i - (x_G - x_s), R_s \sin\alpha_i - (y_G - y_s)) \tag{9}$$

Substituting Eq. (9) into Eq. (8), the instantaneous effective air-gap length can be finally expressed as:

$$e_i(x_G, y_G) = \sqrt{R_s^2 - 2R_s \cdot [\cos\alpha_i \cdot (x_G - x_s) + \sin\alpha_i \cdot (y_G - y_s)] + (x_G - x_s)^2 + (y_G - y_s)^2} - R_r \tag{10}$$

3.2. Calculation of electromagnetic force

There are principally two methods to calculate the electromagnetic force including the electromagnetic torque and UMP due to the air-gap eccentricity. One is obtained by the principle of virtual work or also known as the derivative of the magnetic co-energy method [2, 16, 22]. Another is solved by Maxwell stress tensor method [9, 11]. The latter is often adopted by the researchers who apply the air-gap permeance approach to obtain firstly the radial and tangential flux densities in order to calculate the stress tensor component in normal and tangential direction [10, 21, 23]. The tangential component is often omitted to simplify the calculation according to the assumption that the permeability of the stator and rotor iron is infinite and the motor has smooth poles [21]. In this case, some properties of the UMP cannot be revealed in the simulation results (more details are available in Section 4.2.1). In order to achieve a more realistic UMP values, the magnetic co-energy method is adopted in this article.

The principle of the co-energy approach is to apply the partial differentiation with respect to the relative displacement in order to achieve the force function. For example, the electromagnetic torque T_{em} is calculated by Eq. (11).

$$T_{\mathrm{em}} = \frac{\partial W_m^{'}}{\partial \theta} \tag{11}$$

The co-energy $W_m^{'}$ in the electromagnetic system is often defined by Eq. (12).

$$W_m^{'} = \int_0^{\varepsilon} \phi \cdot \mathrm{d}\varepsilon \tag{12}$$

where ϕ is the linkage magnetic flux and ε is the corresponding MMF drop. In the permeance network described in Section 2.3), the co-energy can be deduced as the sum of co-energies from three parts: the stator and rotor iron part (ir); the leakage part (l) and the air-gap part (a) as described in Eq. (13).

$$W_m^{'} = \sum_{iron} \int_0^{\varepsilon_{\mathrm{ir}}} \phi_{\mathrm{ir}} \cdot \mathrm{d}\varepsilon_{\mathrm{ir}} + \sum_{leakage} \int_0^{\varepsilon_{\mathrm{l}}} \phi_{\mathrm{l}} \cdot \mathrm{d}\varepsilon_{\mathrm{l}} + \sum_{air-gap} \int_0^{\varepsilon_{\mathrm{a}}} \phi_{\mathrm{a}} \cdot \mathrm{d}\varepsilon_{\mathrm{a}} \tag{13}$$

Every linkage magnetic flux passed through each branch are represented by the product of the permeance and MMF drop of each branch in the permeance network. It is calculated in Eq. (14).

$$\phi_k = \varepsilon_k \cdot P_k \tag{14}$$

where ϕ_k is the linkage flux through k_{th} branch in the defined permeance network, ε_k is the corresponding MMF drop and P_k is the permeance value of the k_{th} branch. k is all integer from 1 to N denoted to the branch number of each part. Then Eq. (13) is transformed into Eq. (15):

$$W_m^{'} = \sum_{iron} \int_0^{\varepsilon_{\mathrm{ir}}} \varepsilon_{\mathrm{ir}} \cdot P_{\mathrm{ir}} \cdot \mathrm{d}\varepsilon_{\mathrm{ir}} + \sum_{leakage} \int_0^{\varepsilon_{\mathrm{l}}} \varepsilon_{\mathrm{l}} \cdot P_{\mathrm{l}} \cdot \mathrm{d}\varepsilon_{\mathrm{l}} + \sum_{air-gap} \int_0^{\varepsilon_{\mathrm{a}}} \varepsilon_{\mathrm{a}} \cdot P_{\mathrm{a}} \cdot \mathrm{d}\varepsilon_{\mathrm{a}} \tag{15}$$

Substitution Eq. (15) into Eq. (11), since the MMF drop ε_k of each branch is constant at every simulation step, the derivative of Eq. (15) are treated as the derivative of the permeance value of each part. Considering that the permeances of the stator and rotor iron part P_{ir} don't depend on the variation of the rotor relative displacements directly and the permeances of the leakage part P_{l} are constant values so that the derivatives of the first two terms in Eq. (15) equal to zero. It implies the fact that the energy conversion between the electromagnetic part and the mechanical part only happens in the air-gap area [12]. Therefore Eq. (11) is developed into Eq. (16) :

$$T_{\mathrm{em}} = \sum_{air-gap} \int_0^{\varepsilon_a} \frac{\partial P_a}{\partial \theta} \cdot \varepsilon_a \cdot \mathrm{d}\varepsilon_a = \sum_{air-gap} \frac{\varepsilon_a^2}{2} \cdot \frac{\partial P_a}{\partial \theta} \tag{16}$$

As introduced in the former sections the branches in the air-gap are related to each stator tooth i and rotor tooth j. In this way the air-gap permeances and corresponding MMF drops are defined as $P_a = P_{ij}$ and $\varepsilon_a = \varepsilon_{ij}$. Since the relative rotation angle between each stator and rotor teeth is represented by θ_{ij}, the expression of Eq. (16) in the whole air-gap area becomes:

$$T_{\mathrm{em}} = \frac{1}{2} \sum_i^{n_s} \sum_j^{n_r} \frac{\partial P_{ij}}{\partial \theta_{ij}} \varepsilon_{ij}^2 \tag{17}$$

The partial derivation of the Eq. (5) about the relative rotation angle θ_{ij} appears as:

$$\frac{\partial P_{ij}(x_G, y_G, \theta_{ij})}{\partial \theta_{ij}} = \frac{P_{\mathrm{maxc}}}{e_i(x_G, y_G)} \cdot \frac{df_p(\theta_{ij})}{\mathrm{d}\theta_{ij}} \tag{18}$$

The second term $\frac{\mathrm{d}f_p(\theta_{ij})}{\mathrm{d}\theta_{ij}}$ is deduced in Eq. (C.4) from Appendix C. In the same way, magnetic radial forces (UMP) due to the eccentricity are achieved by taking the derivative of the magnetic co-energy about their relative displacement along the x and y directions:

$$\begin{aligned} F_{\mathrm{emx}} &= \frac{1}{2} \sum_i^{n_s} \sum_j^{n_r} \frac{\partial P_{ij}}{\partial \tilde{x}} \varepsilon_{ij}^2 \\ F_{\mathrm{emy}} &= \frac{1}{2} \sum_i^{n_s} \sum_j^{n_r} \frac{\partial P_{ij}}{\partial \tilde{y}} \varepsilon_{ij}^2 \end{aligned} \tag{19}$$

From Fig. 7, it can be seen that the effective air-gap length actually depends on the variation of the relative displacements between the stator center O_S and rotor geometric center O_G. In order to obtain their variation, Eq. (10) needs to be transformed into the coordinate of $x_s o_s y_s$ in Fig. 7 with the relative displacements along two directions $\tilde{x}$ and $\tilde{y}$ defined as:

$$\begin{aligned} \tilde{x} &= x_G - x_s \\ \tilde{y} &= y_G - y_s \end{aligned} \tag{20}$$

Therefore the partial differentiation of Eq. (5) about the relative displacement $\tilde{x}$ is deduced as:

$$\begin{aligned} \frac{\partial P_{ij}(\tilde{x},\tilde{y},\theta_{ij})}{\partial \tilde{x}} &= \frac{\partial(\frac{1}{e_i(\tilde{x},\tilde{y})})}{\partial \tilde{x}} \cdot P_{\mathrm{maxc}} \cdot f_p(\theta_{ij}) \\ &= -\frac{1}{e_i(\tilde{x},\tilde{y})} \cdot \frac{\partial e_i(\tilde{x},\tilde{y})}{\partial \tilde{x}} \cdot P_{ij}(\tilde{x},\tilde{y},\theta_{ij}) \end{aligned} \tag{21}$$

Substitution from Eq. (10) in the coordinate of $x_s O_s y_s$, the second term on the right side of Eq. (21) is developed as:

$$\frac{\partial e_i(\tilde{x},\tilde{y})}{\partial \tilde{x}} = \frac{1}{2} \cdot \frac{-2R_s \mathrm{cos}\alpha_i + 2\tilde{x}}{\sqrt{R_s^2 - 2R_s(\mathrm{cos}\alpha_i \cdot \tilde{x} + \mathrm{sin}\alpha_i \cdot \tilde{y}) + \tilde{x}^2 + \tilde{y}^2}} \tag{22}$$

The partial differentiation of Eq. (5) about $\tilde{y}$ can be deduced in the same way.

3.3. Calculation about the derivative of the magnetic flux

By substituting Eq. (3) into Eq. (4), the global differential equation about the coupling of electro-magnetic model becomes:

$$\mathbf{R} \cdot \mathbf{I}(t) + \frac{\mathrm{d}(\mathbf{Gg} \cdot \mathbf{XX}(\mathbf{X}) \cdot \mathbf{ZZ} \cdot \mathbf{I}(t))}{\mathrm{d}t} = \mathbf{V}(t) \tag{23}$$

The second term about the derivative of the magnetic flux in Eq. (23) is developed as:

$$\begin{aligned} &\frac{\mathrm{d}(\mathbf{Gg} \cdot \mathbf{XX}(\mathbf{X}) \cdot \mathbf{ZZ} \cdot \mathbf{I}(t))}{\mathrm{d}t} \\ =&\mathbf{Gg} \cdot \frac{\mathrm{d}\mathbf{XX}(\mathbf{X})}{\mathrm{d}\mathbf{t}} \cdot \mathbf{ZZ} \cdot \mathbf{I}(t) + \mathbf{Gg} \cdot \mathbf{XX}(\mathbf{X}) \cdot \mathbf{ZZ} \cdot \frac{\mathrm{d}\mathbf{I}(t)}{\mathrm{d}t} \end{aligned} \tag{24}$$

In Eq. (24), $\mathbf{I}(t)$ is the state vector so the derivative of this term is used for solving the differential equation. As mentioned in Section 2.3, the first term $\mathbf{XX}(\mathbf{X})$ is a matrix of permeance deduced as the function of the shaft rotation angle θ and the rotor center displacements x_r, y_r so that $\mathbf{XX}(\mathbf{X})$ is simplified as $\mathbf{XX}(\theta, x_r, y_r)$. Thanks to the angular approach, its derivative about the time is deduced in Eq. (25):

$$\begin{aligned} \frac{\mathrm{d}\mathbf{XX}(\theta, x_r, y_r)}{\mathrm{d}t} &= \frac{\mathrm{d}\mathbf{XX}(\theta, x_r, y_r)}{\mathrm{d}\theta} \cdot \frac{\mathrm{d}\theta}{\mathrm{d}t} \\ &= (\frac{\partial \mathbf{XX}}{\partial \theta} + \frac{\partial \mathbf{XX}}{\partial x_r} \cdot \frac{\mathrm{d}x_r}{\mathrm{d}\theta} + \frac{\partial \mathbf{XX}}{\partial y_r} \cdot \frac{\mathrm{d}y_r}{\mathrm{d}\theta}) \cdot \dot{\theta}(t) \end{aligned} \tag{25}$$

Since the rotor center displacements and their corresponding instantaneous translation speeds are available from the state vectors, their derivative about the rotation angle are calculated in Eq. (26) by applying again the chain rule :

$$\begin{aligned} \frac{\mathrm{d}x_r(t)}{\mathrm{d}\theta} &= \frac{\mathrm{d}x_r(t)}{\mathrm{d}t} \cdot \frac{\mathrm{d}t}{\mathrm{d}\theta} \\ \frac{\mathrm{d}y_r(t)}{\mathrm{d}\theta} &= \frac{\mathrm{d}y_r(t)}{\mathrm{d}t} \cdot \frac{\mathrm{d}t}{\mathrm{d}\theta} \end{aligned} \tag{26}$$

Substitution Eq. (26) into Eq. (25), the derivative of the permeance matrix $\mathbf{XX}$ about the time is achieved in Eq. (27).

$$\frac{\mathrm{d}\mathbf{XX}(\theta, x_r, y_r)}{\mathrm{d}t} = \frac{\partial \mathbf{XX}}{\partial \theta} \cdot \dot{\theta}(t) + \frac{\partial \mathbf{XX}}{\partial x_r} \cdot \dot{x_r}(t) + \frac{\partial \mathbf{XX}}{\partial y_r} \cdot \dot{y_r}(t) \tag{27}$$

where $\dot{\theta}(t)$, $\dot{x_r}(t)$ and $\dot{y_r}(t)$ are respectively the instantaneous angular and translation speeds of the rotor center.

4. Simulation results and discussion

4.1. *Model verification in the quasi-static regime*

This model is firstly verified by comparing its simulation results in the case without input eccentricity with the reference machine data provided by our industrial partner Nidec-Leroy Somer. Those reference data are calculated at each operating point from a company internal software based on MEC while the simulation results of our model are achieved from the steady state to realize the verification in the quasi-static regime. Therefore two motor characteristic curves about the relation of the Torque-Speed and the Current-Speed are plotted separately in Fig. 8a and Fig. 8b. The reference machine is a three phases, double squirrel cage induction motor. All the machine parameters are available in Table D.1 and its mechanical characteristics are listed in Table D.2 from Appendix D.

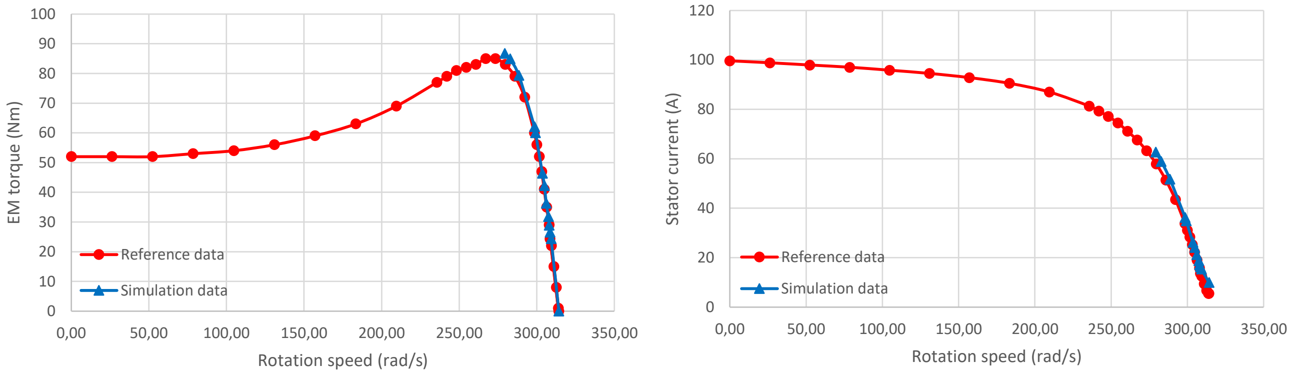

(a) Torque vs Speed

(b) Current vs Speed

Fig. 8. Induction motor characteristic curve

By applying a load torque in the mechanical subsystem, this model simulates the corresponding operating point which produces the same value of the electromagnetic torque to balance the system. Each simulation starts with all the state vectors assumed to be zero. It should be noted that with this coupled model, only the working points with small slips from the motor characteristic curves can be simulated for the reason that they belong to the stable operation range of the motor's operation mode. In the induction motor, the motor slip (s) is the difference between the shaft rotation speed (ω_r) and the synchronous speed of the power supply (ω_s) as defined in Eq. (28).

$$s = \frac{\omega_s - \omega_r}{\omega_s} \tag{28}$$

That's why in Fig. 8, only the half curve is plotted from the simulation data in each subfigure.

Since there are no input eccentricities, the simulation results of UMP two components (F_{emx} and F_{emy}) both converge to 0. There is a good agreement between two curves in the common part. Every point from the blue curve in Fig. 8a is obtained from the average value of the generated electromagnetic torque during the steady state of each simulation as shown in Fig. 9a while each current value from Fig. 8b is the effective value calculated from the amplitude value illustrated in Fig. 9b. The simulation results plotted in Fig. 9 are simulated at the rated operation state. The fluctuation of the instantaneous electromagnetic torque value illustrated in Fig. 9a is introduced by the slot effects on the dynamic behavior. Focusing on the operation range of the electrical machine, some differences begin to appear between the two curves with the increase of the motor slip defined in Eq. (28). This is due to the simplification of the rotor cage geometry where the double cage rotor structure in the real machine is reduced to the single cage rotor by reserving the same slot surface. The skin effect of the rotor current is also neglected so the difference becomes bigger with the increase of the motor slip. Considering that the vibration analysis need to be effectuated during the motor's operation mode, these comparison results are able to validate this multiphysics model in the case without input eccentricity in the quasi-static regime.

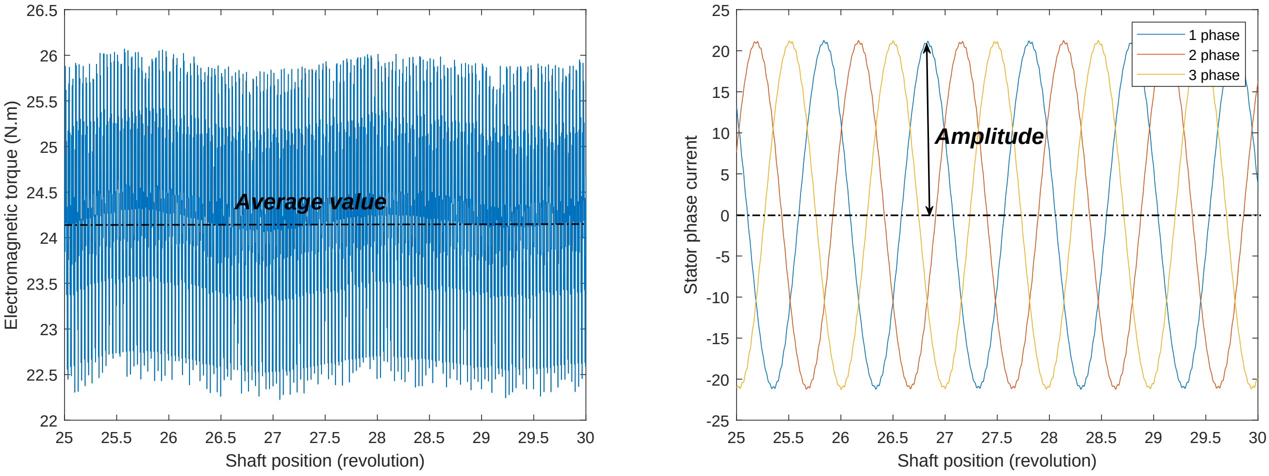

(a) Variation of Electromagnetic torque

(b) Variation of stator phase currents

Fig. 9. Simulation results computed without input eccentricity as a function of the shaft position

The second verification in the quasi-static regime is effectuated in the case with the input static eccentricity of different values set up along the x-axis at the rated operating point. It is realized by comparing the simulation results of UMP along the direction of the input eccentricity in the steady state with those calculated from an open source software Finite Element Method Magnetics (FEMM) [24]. To simplify the analysis, the input eccentricity value is defined as the percentage of the air-gap average length Ee. As it is illustrated in Fig. 10, those two simulation results about F_{emx} are well consistent and the maximum error between the two is around 3.8%. It demonstrates that this multiphysics model is also validated in the case with the eccentricity in the quasi-static regime.

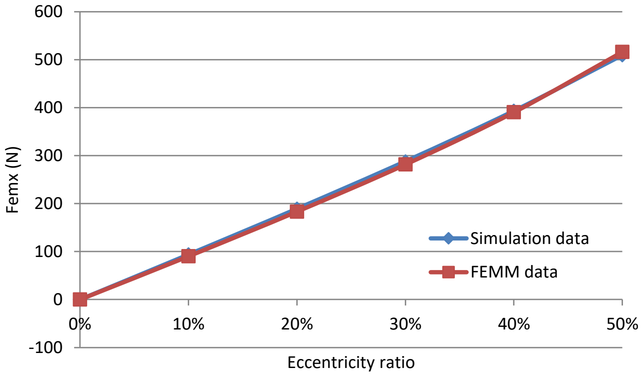

Fig. 10. Comparison of simulation results about F_{emx} at the rated operating point

4.2. Study of the case with 10%Ee input static eccentricity

The machine mentioned in Section 4.1 is adopted to study the influence of the rotor eccentricity on the dynamic behavior of the electrical machine. At this first step, 10%Ee static eccentricity is set up along the horizontal axis (x-axis) by modifying the coordinate of the stator center O_S into:

$$\begin{aligned} x_s &= -10\%Ee \\ y_s &= 0 \end{aligned} \tag{29}$$

Two operating conditions are investigated in this section. The first is at the rated rotation speed 309.26 rad·s^{-1} and the second is chosen to be next to the operating point of the maximum torque from Fig. 8a with the rotation speed equaled to 289.20 rad·s^{-1}. All the simulations are performed for firstly 50 revolutions to attain the steady state and then the results of the next 1000 revolutions are analyzed to avoid the transient state influence.

The simulation results of UMP in the steady state with 10%Ee input eccentricity for the two operating points are shown separately in Fig. 11. It can be seen from both two graphs that with an input static eccentricity, two components of UMP are converged to different constant values respectively and fluctuate around them with similar amplitudes. These results conform to the first conclusion in [10]. Their amplitudes are increased with the increase of the motor slip. Since F_{emx} is the main UMP component force generated from the input eccentricity, its average value in this direction is also increased. This is due to that as the motor slip increases, the induced current in the magnetic field becomes bigger as well as the magnetic flux through the air gap, resulting in an increase in the generated electromagnetic forces according to Section 3.2. Some other phenomena about UMP can be investigated and are going to be discussed hereafter in two parts: physical characteristics and frequency analysis.

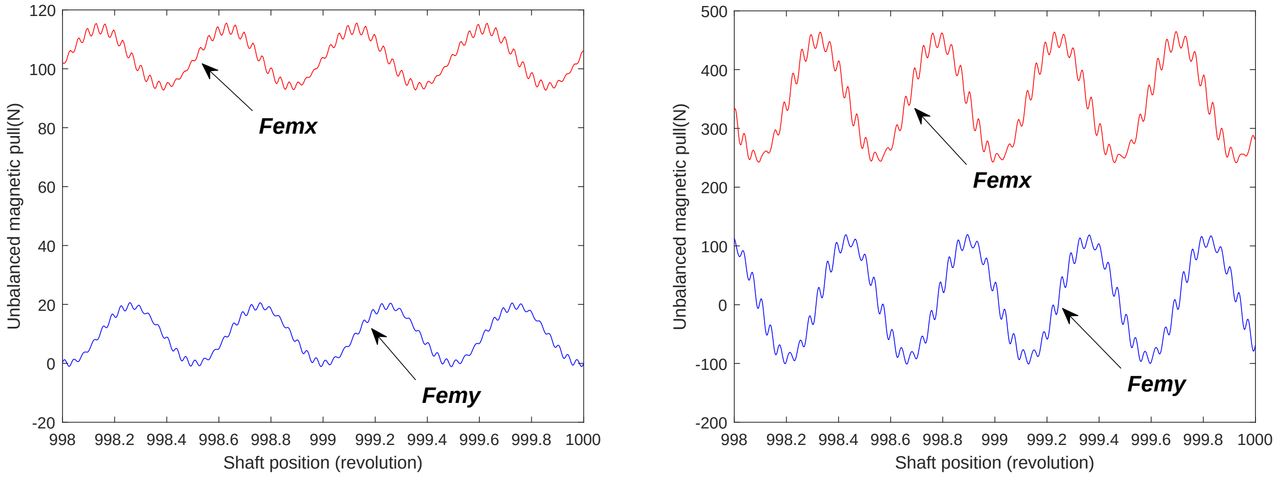

(a) ω_r = 309.26 rad·s^{-1} **(b)** ω_r = 289.20 rad·s^{-1}

Fig. 11. Variation of UMP with 10%Ee eccentricity in the last two revolutions

4.2.1. Physical characteristics

From Fig. 11, the average value of F_{emx} is larger than that of F_{emy} because the input eccentricity is placed on x-axis. However it is also found that the steady component of UMP projected to the vertical direction F_{emy}

isn't zero. This means the UMP resultant force doesn't act along the direction of the initial smallest air-gap as we usually considered but it rotates slightly from the narrowest air-gap position with a certain offset angle. This angle can be identified more clearly in the polar diagram of UMP shown in Fig. 12a by plotting the variation of F_{emy} as a function of F_{emx} in a polar coordinate. Since the UMP variation has some oscillation components, the arrow in Fig. 12a is plotted by the average value of UMP to show its average magnitude and the small orbit at the top of the arrow illustrates the arrow's end trajectory during one shaft revolution in order to display the variation of the UMP magnitude and offset angle in the xoy section. This phenomenon is generated by the effects of equalizing currents induced in the rotor cage due to the eccentricity. As explained in [25] based on a FEM model, these currents reduce the amplitude of the force and change the direction of the force from the direction of the minimum air gap. Thus, our multiphysics model can be confirmed by displaying this phenomenon in the simulation results of UMP.

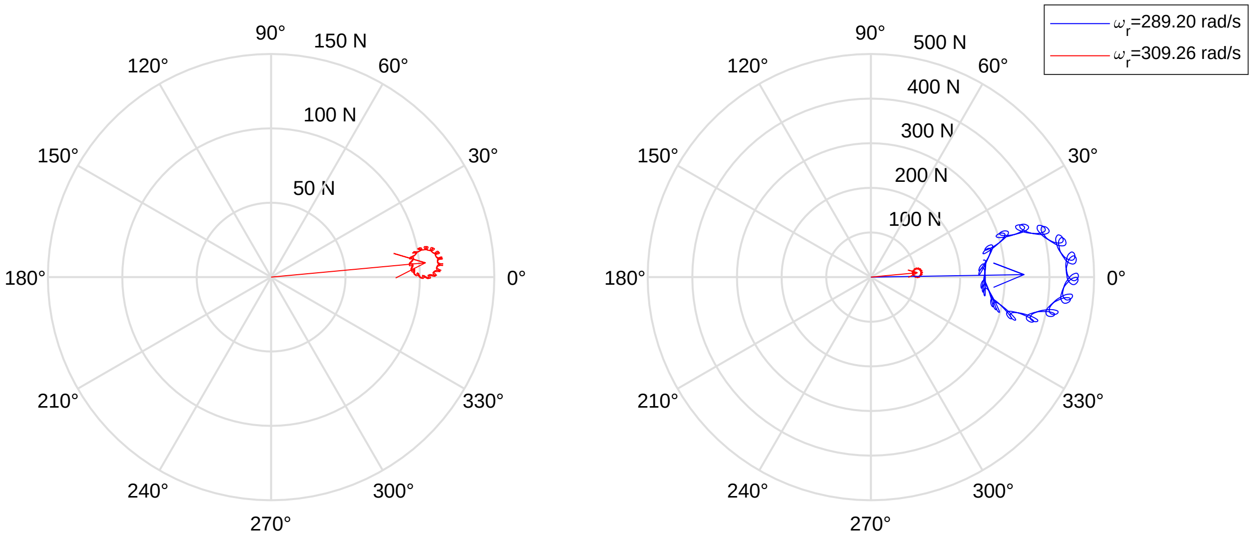

(a)

(b)

Fig. 12. Polar diagram of UMP with 10%Ee eccentricity in the last shaft revolution

Comparing the polar diagrams of UMP at different operating points in Fig. 12b, it is shown that the UMP resultant force magnitude increases and the orbit becomes bigger in two directions simultaneously with the increase of the motor slip but meanwhile its average offset angle decreases. It demonstrates that the variation range of the UMP magnitude and its offset angle is increased at the same time and it indicates that the UMP generated in the case with a bigger motor slip tends to fluctuate around the position of the set-up eccentricity with larger oscillations.

Due to the UMP fluctuations in its magnitude and direction, the generated radial displacements of the rotor geometric center can be described as an orbit. Fig. 13 gives an overview of the relative positions about this rotor center orbit (in red), the stator center O_S and the rotor center initial position O. Since O_G (the red point in the left schema) is not fixed at its initial position O (the black point), it finally rotates around the area close to the black point. It is more clearly if the center zone in the dotted rectangle is zoomed in the right schema of Fig. 13. As defined in Eq. (29), the distance between O_S and O represents the input 10%Ee static eccentricity along x-axis while the small red orbit close to O shows the real motion of O_G due to the generated UMP.

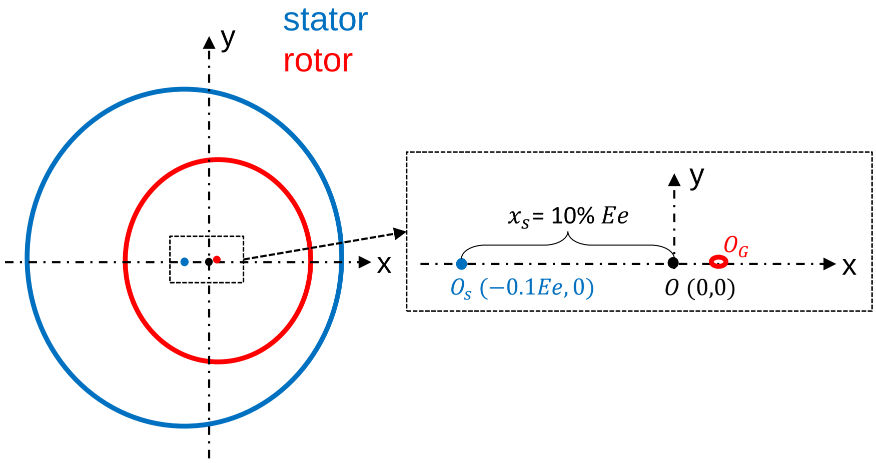

Fig. 13. Rotor center orbit in xoy section with 10%Ee eccentricity

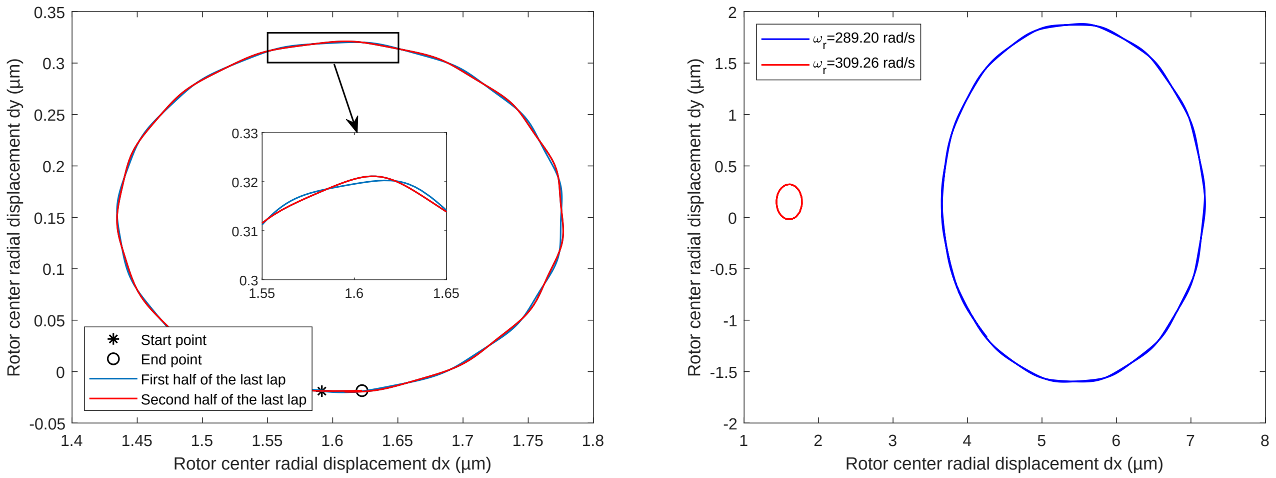

(a) ω_r = 309.26 rad $\cdot$ s^{-1}

(b) Comparison of two orbits

Fig. 14. Rotor center orbit in xoy section with 10%Ee eccentricity

The simulation result about this rotor center orbit at the rated operation state during the last shaft revolution is plotted in Fig. 14a. It is shown that the rotor center rotates in two slightly circumferential shifted orbits that are plotted in two different colors. There are about 15 ripple waveforms as displayed in the zoom part of Fig. 14a around each orbit and they are almost evenly distributed around the entire circumference which means that during the last shaft revolution there are totally 30 ripple waveforms corresponding to the number of the rotor bars. It reflects how slot effects act on the dynamic behavior of the induction machine. Start and end points of this last revolution don't coincide. Their distance and the shift between the two orbits are introduced by the motor slip. The comparison of two orbits simulated at two operating points is illustrated in Fig. 14b. Thanks to the strong coupling in this multiphysics model, the nonlinear variation of the rotor center radial displacements under the UMP generated from the cases with the same input eccentricity but at different operating points are achieved naturally from the simulation results.

4.2.2. Frequency analysis

Frequency responses presented in this paper are obtained by applying the Fast Fourier Transform analysis on the results over 1000 revolutions in order to achieve precision of the frequency value. The UMP along x direction is chosen to perform the frequency analysis since F_{emx} is the main UMP component force. In order to provide order analysis, the traditional frequency spectral analysis is also realized in the angular domain with the unit defined as "event per shaft revolution ($\text{ev} \cdot \text{rev}^{-1}$)". The transform relationship between the angular frequency f_θ and the traditional frequency f is defined in Eq. (30).

$$f_\theta(\text{ev} \cdot \text{rev}^{-1}) = 2 * \pi * \frac{f(\text{Hz})}{\omega_r(\text{rad} \cdot \text{s}^{-1})} \tag{30}$$

Therefore the power supply frequency 50 Hz is shown as 1.016 $\text{ev} \cdot \text{rev}^{-1}$ and 1.0863 $\text{ev} \cdot \text{rev}^{-1}$ respectively in the angular spectrum for the two operating points.

Their frequency spectrum in the angular and time domain at two rotation speeds are illustrated separately in Fig. 15 and Fig. 16. Four characteristic frequencies could be evidently recognized from all of the four spectrum. Taken the rated state in Fig. 15 as an example, they are: the double supply frequency $2f_s = 2.032\ \text{ev} \cdot \text{rev}^{-1}$; slot harmonic equals to the rotor teeth number $f_{\text{sh}} = 30\ \text{ev} \cdot \text{rev}^{-1}$ and the other two sideband frequencies on either side of the slot harmonic $f_{\text{sh}} \pm 2f_s$. According to the conclusion stated in [26], a homo-polar flux due to the rotor static eccentricity is generated in the two pole squirrel cage induction machine and this homo-polar component will cause a vibration component of UMP with double supply frequency $2f_s$. Therefore, the existence of this characteristic frequency due to the input static eccentricity allows us to further validate our model.

Comparing the two angular spectrum at different rotation speeds (Fig. 15a and Fig. 16a), the frequency peak corresponded to f_{sh} appear at the same place 30 $\text{ev} \cdot \text{rev}^{-1}$ however the others associated with $2f_s$ displaced with the variation of the rotation speed. In contrary, the frequency peak referred to $2f_s$ are identified at the same position 100 Hz in the two traditional spectrum from Fig. 15b and Fig. 16b while the others change their values with the augmentation of the rotation speed. It implies that the slot harmonic f_{sh} is an angular cyclic phenomenon while the double supply frequency $2f_s$ is a temporal cyclic phenomenon and the frequency combinations between the two $f_{\text{sh}} \pm 2f_s$ are assumed to be the modulation between the angular and temporal phenomenon. Since the rotor eccentricity is the disturbance in the electrical machine, this similar signal modulation demonstrates that UMP produced by the input static eccentricity is generally acted as a steady pull to the whole system. The second harmonic of the double supply frequency and its modulation with the slot harmonic arise in Fig. 16 with the increase of the motor slip and this is explained in Section 4.2.3.

Similarly these characteristic frequencies can also be detected in the corresponding electromagnetic torque by comparing its angular spectrum simulated in the case with and without eccentricity shown in Fig. 17. Double supply frequency 2.032 $\text{ev} \cdot \text{rev}^{-1}$ and its modulation with the slot harmonic 27.97 $\text{ev} \cdot \text{rev}^{-1}$ are only identified in the case with $10\% Ee$ eccentricity. It reflects that the rotor radial displacements also influence its rotational movement.

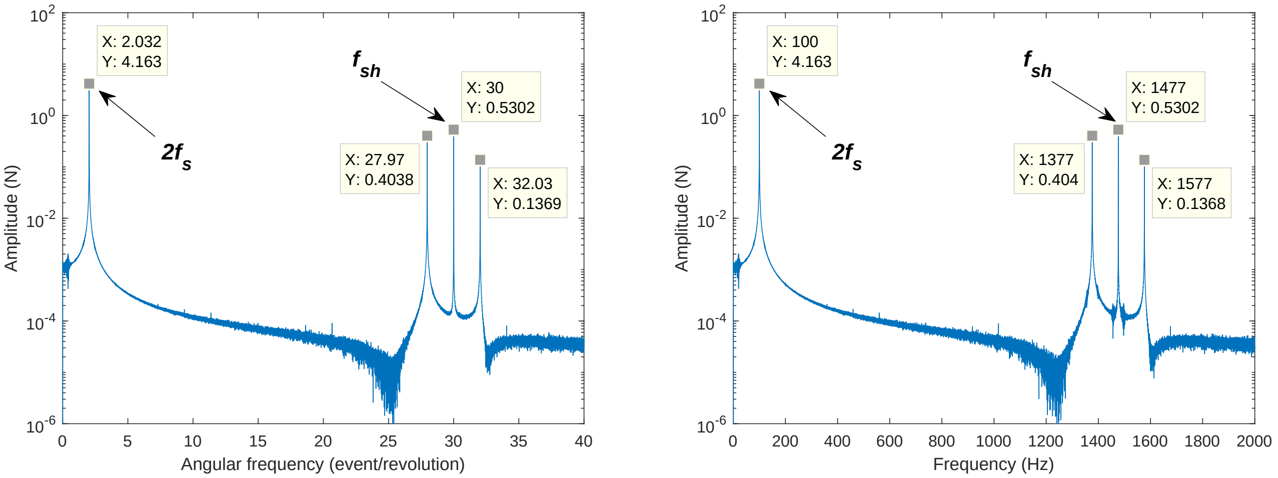

(a) Angular spectrum **(b)** Traditional spectrum

Fig. 15. Frequency spectrum of UMP along x direction with 10%Ee eccentricity at $\omega_r = 309.26$ rad · s^{-1}.

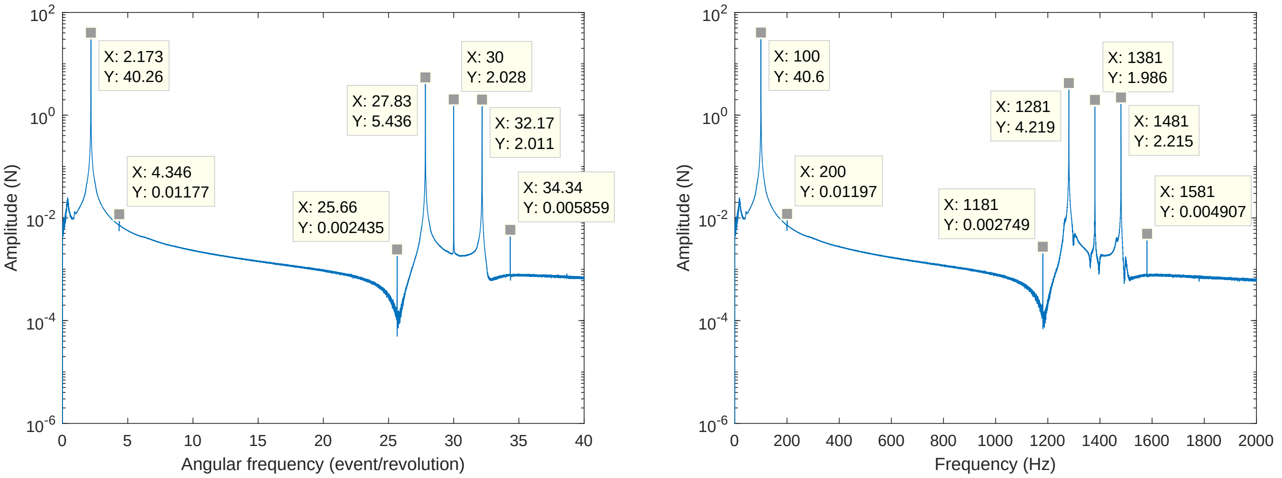

(a) Angular spectrum **(b)** Traditional spectrum

Fig. 16. Frequency spectrum of UMP along x direction with 10%Ee eccentricity at $\omega_r = 289.20$ rad · s^{-1}.

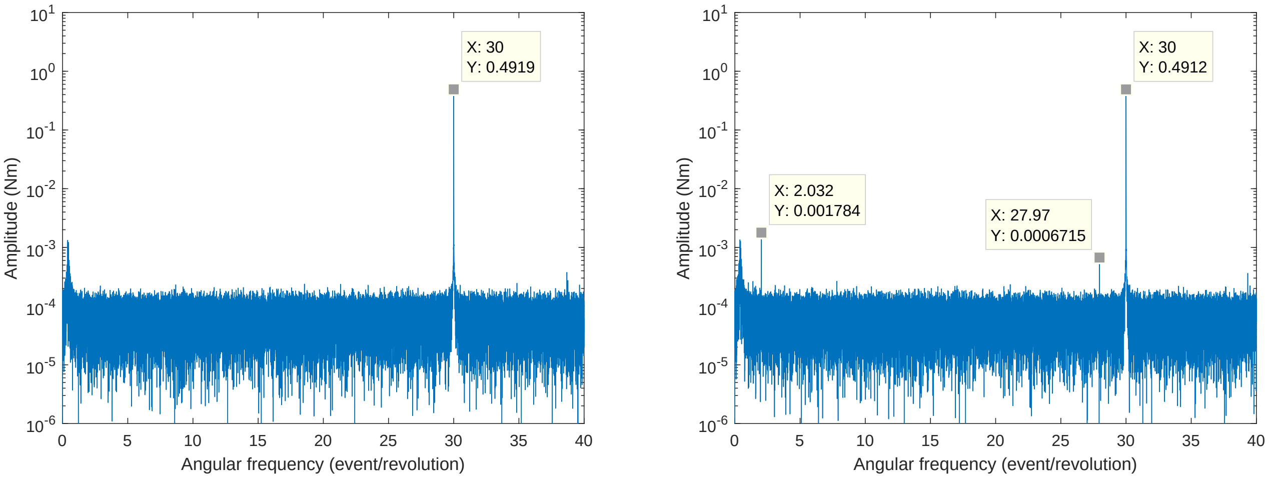

(a) Without eccentricity **(b)** With 10%Ee eccentricity

Fig. 17. Angular spectrum of electromagnetic torque at the rated operation state

4.2.3. Simulation in non-stationary operating conditions

As mentioned in Section 4.1, a constant load torque is applied to simulate a given operating point from the motor characteristic curve in Fig. 8a in steady state. In this section, a load torque that increases linearly with the shaft revolution as shown in Fig. 18a is set up in this multiphysics model to perform the simulation with 10%Ee input eccentricity in non-stationary operating conditions. The simulation results about the variation of the instantaneous angular speed and the electromagnetic torque are illustrated separately in Fig. 18b and Fig. 18c as the function of the shaft position. The average value of the electromagnetic torque always equals to the applied load torque but meanwhile its fluctuation amplitude is increased gradually with the augmentation of the load torque due to the increase of the motor slip as explained in the beginning of Section 4.2. The increased fluctuation amplitude appears more evident in the variation of the UMP along x direction displayed in Fig. 19. By applying a short-angle Fourier transform, its angular spectrogram is shown in Fig. 20. The four characteristic frequencies discussed in Section 4.2.2 are revealed clearly in the spectrogram of F_{emx}. With the increase of the motor slip, the amplitudes of each frequency components increased and some more harmonics about the $2f_s$ and their modulations with f_{sh} appear for large motor slip (see arrows pointing parts in Fig. 20) corresponding to the phenomenon presented in Fig. 16. It clearly indicates that the same input eccentricity value will have more evident impact on the mechanical system with the increase of the motor slip. With the increase of the load torque, the UMP not only increases its magnitude but also induces more harmonics in the whole structure which potentially increases the risk of the resonance.

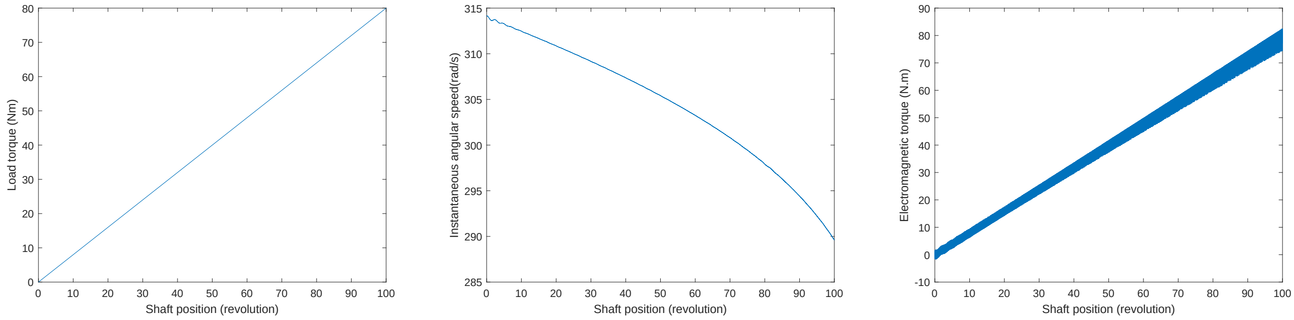

(a) Load torque **(b)** Instananous angular speed **(c)** Electromagnetic torque

Fig. 18. Simulation results variation in non-stationary operating conditions

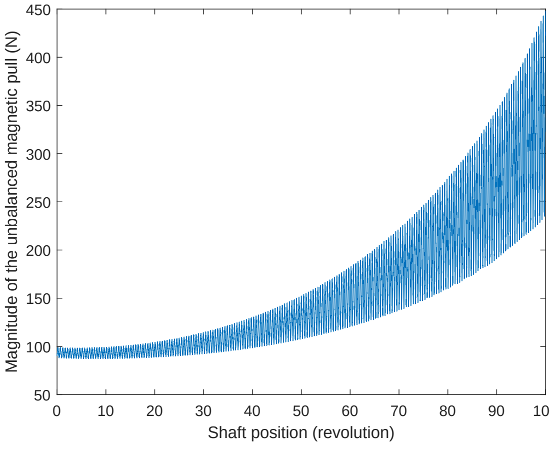

Fig. 19. Variation of UMP along x direction

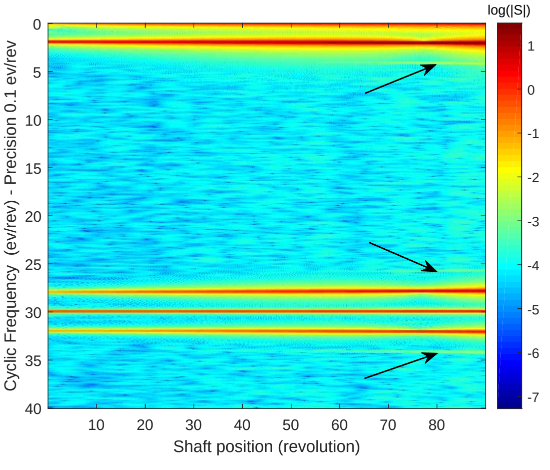

Fig. 20. Short angle spectrum of UMP along x direction

4.3. Influence of the input eccentricity amplitude variation

The polar diagrams of UMP with 3 different input static eccentricities at the rated operating point are plotted in Fig. 21. As introduced in Section 4.2.1, the arrows represent the average value of each UMP magnitude while the orbits at the end of each arrow illustrate the variation of the UMP and its offset angle during one shaft revolution. It is shown that at the rated operating point ($\omega_r = 309.26\ \mathrm{rad}\cdot\mathrm{s}^{-1}$), the UMP magnitude and the fluctuation range of UMP and its offset angle increase proportionally with the augmentation of the input static eccentricity values while their average offset angles remain the same.

The variation of the instantaneous rotation speeds simulated with those three eccentricity values are illustrated in Fig. 22. Although the rotation speeds all converge to the same constant value, it can be seen clearly that their variations with the shaft rotation angle become more fluctuated. In order to identify this fluctuation component, their angular spectrum are compared in Fig. 23. As discussed in Section 4.2.2, the four characteristic frequencies identified in UMP spectrum are also recognized in all of three rotation speed spectrum but beside of the slot harmonic f_{sh} associated with the motor's geometry, the amplitudes of other frequency components increase evidently with the augmentation of the input eccentricity value. It signifies that the radial eccentricity do have the influence on the rotation speed variation and this impact becomes more evident with the increase of the eccentricity value. Relatively, the amplitude increase of the double supply frequency and of the sideband frequencies in the rotation speed spectrum reflects the increase of the eccentricity amplitudes.

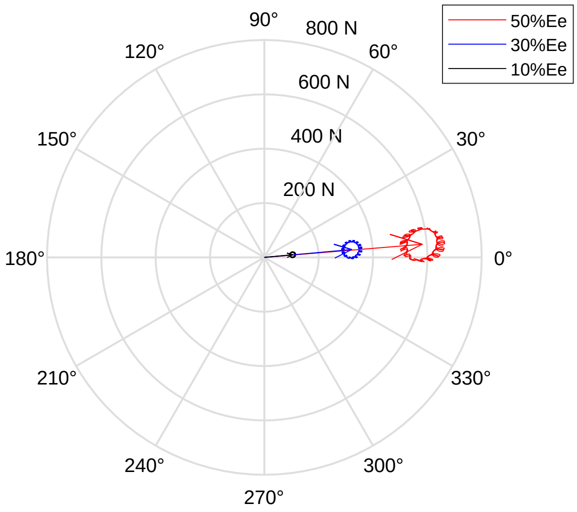

Fig. 21. Polar diagram of UMP with different eccentricities at the rated operating point

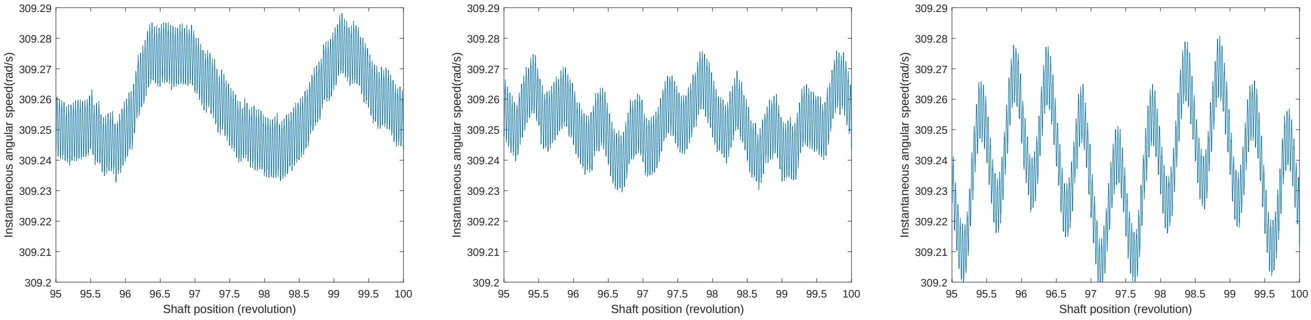

(a) With 10%Ee eccentricity **(b)** With 30%E_e eccentricity **(c)** With 50%E_e eccentricity

Fig. 22. Variation of instantaneous rotation speed at the rated operation state

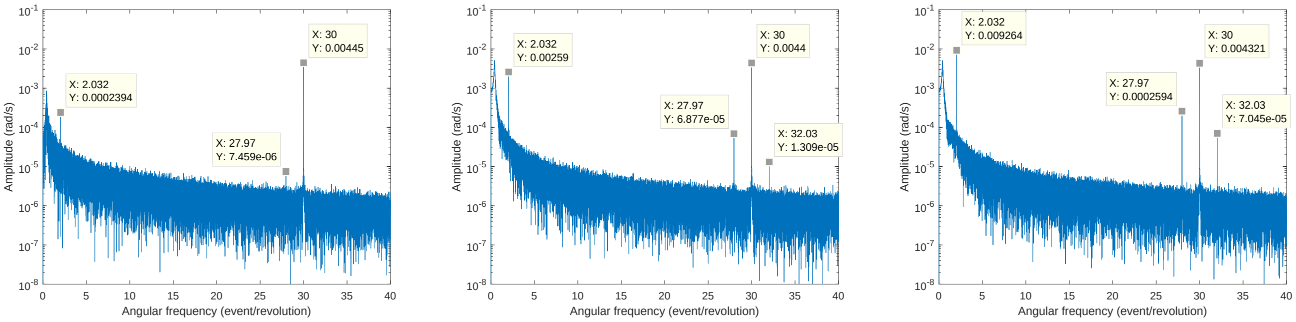

(a) With 10%Ee eccentricity **(b)** With 30%E_e eccentricity **(c)** With 50%E_e eccentricity

Fig. 23. Angular spectrum of instantaneous rotation speed at the rated operation state

5. Conclusions

An angular based model for calculating UMP in a 3-phase squirrel cage induction machine is developed in this paper by defining the effective air-gap length as a function of the rotor geometric center coordinates. This model is inserted into a multiphysics electric machine model to reinforce the electro-magneto-mechanic interaction in order to study the influence of the rotor eccentricity on the dynamic behavior of an induction machine. This multiphysics model allows us to perform a longtime simulation even in non-stationary operating conditions with less calculating efforts when comparing with the traditional numerical model. The model is validated in the quasi-static regime by comparing its simulation results with the reference data calculated by the traditional numerical model in the case with and without the eccentricity.

Several interesting phenomena about UMP are identified from the analysis of its simulation results with 10%E_e input static eccentricity. Some of them have been confirmed in the previous literatures to allow us validate the reliability of this multiphysics model. The rotor eccentricity impacts at different operating points and the influence of its amplitude variation are discussed separately by analyzing other simulation results apart from the UMP. Actually every simulation results associated with three fields in this multiphysics model are available to predict the dynamic behaviors of the whole system. For example, the stator phase current could be used to understand the presence of the eccentricity using Motor Current Signal Analysis. For the sake of clarity, only the mechanical variables have been analyzed in this paper and the following results can be drawn:

- The UMP generated by the input static eccentricity is acted as a steady pull to the rotor therefore two characteristic frequencies and their combinations are identified from the spectrum of UMP and also from the spectrum of the electromagnetic torque which indicates the connection between the rotor radial movement and its rotational movement. However this steady pull doesn't point to the narrowest air-gap direction but rotates from this direction with an offset angle. All these phenomena are also revealed from the simulated rotor center orbits.

- Based on the analysis at different operating points, it implies that with the increase of the motor slip, the same input eccentricity value will have more evident impact on the mechanical system: the generated UMP not only increases its magnitude but also induces more harmonics in the whole structure which potentially increases the risk of resonance.

- Based on the evaluation about the influence of eccentricity amplitude variations at the rated operating point, it can be seen that the radial eccentricity impact is also revealed in the rotation speed variation and this impact becomes more evident with the increase of the eccentricity value. This provides a theory evidence for comparing the eccentricity amplitude from the spectrum analysis of the rotation speed.

Since the saturation effect is not considered in the present model, the simulated UMP values could be overestimated. In order to study its influence, the magnetic saturation effect will be added to this model in future works. Overall this multiphysics model with strong electro-magneto-mechanical coupling is of great importance to study the influence of the rotor eccentricity on the entire dynamic behaviors of the electrical motor and it can help us to get a better understanding about the electro-magneto-mechanic interaction inside electrical machines.

Acknowledgments

This work was supported by the French National Agency of Research and Technology (ANRT), CIFRE [grant number 2017/1333] and Company Nidec Leroy Somer. Special acknowledgments are dedicated to Mr. Jacques SAINT-MICHEL for his explanation about the origin of the UMP offset angle.

Appendix A. Setting up different types of input eccentricities

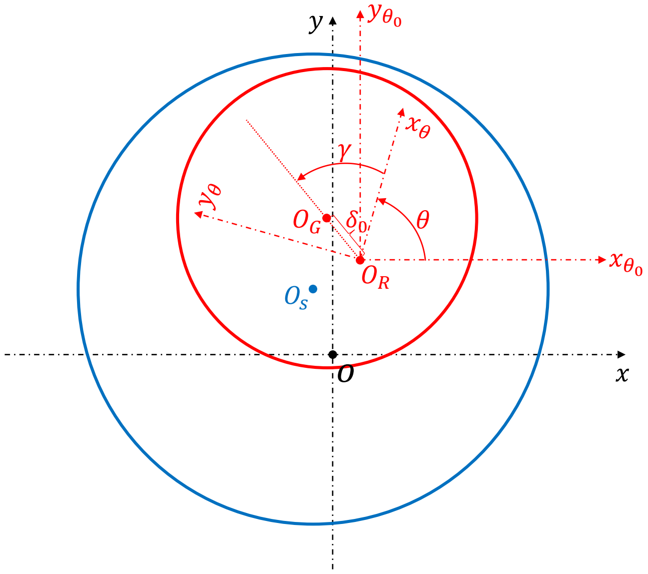

Fig. A.1. Cross-sectional view of an eccentric rotor

Since the mechanical modeling is based on the rotor part as mentioned in Section 2.2, the reference coordinate system xOy in Fig. A.1. is established by taking the initial position of the rotor center as the origin point O. This initial position is defined before the start of the electrical machine's operation. At this moment, the coordinate of the stator center $O_S(x_s, y_s)$ is used to present its position and the value of the initial input static eccentricity. Once the motor begins to operate, due to the strong coupling with the mechanical part, the rotor geometric center isn't fixed at its initial point O but moves to another position which is assumed to be the point O_R. Its coordinate (x_r, y_r) in the reference coordinate system is considered as one of the state variables in this multiphysics model so that it is updated at every rotor rotation angle θ under the influence of the UMP generated inside of the electrical machine or the effect of the radial external force on the structure.

If the rotor isn't perfectly cylindrical along its axis due to some manufacturing faults or the rotor does a dynamic whirling motion inside of the stator, then its geometric center O_G of the middle section doesn't coincide with its rotation center O_R but rotates around it in a similar crankshaft movement with the radius δ_0 and a constant phase shift angle γ. The rotational coordinate $x_\theta O_R y_\theta$ in Fig. A.1 rotates around the rotation center O_R from the initial position presented by the coordinate $x_{\theta_0} O_R y_{\theta_0}$ which is translated parallel to the reference coordinate xOy. This synchronism whirling movement of O_G is described by the vector $\mathbf{O_R O_G} = (\delta_0 * \cos(\theta+\gamma), \delta_0 * \sin(\theta+\gamma))$ in the coordinate system $x_{\theta_0} O_R y_{\theta_0}$. Considering the vector $\mathbf{OO_R} = (x_r, y_r)$, the position of O_G is calculated in the form of $\mathbf{O_G O}$ as Eq. (A.1) .

$$\mathbf{OO_G} = \mathbf{OO_R} + \mathbf{O_R O_G} = (\delta_0 * \cos(\theta+\gamma) + x_r, \delta_0 * \sin(\theta+\gamma) + y_r) \tag{A.1}$$

Then the coordinate of the rotor geometric center position $O_G(x_G, y_G)$ in the reference coordinate system is deduced from Eq. (A.2):

$$\begin{aligned} x_G &= x_r + \delta_0 * \cos(\theta+\gamma) \\ y_G &= y_r + \delta_0 * \sin(\theta+\gamma) \end{aligned} \tag{A.2}$$

This coordinate is adopted to calculate the instantaneous effective air-gap length in the Section 3.1. It can be seen clearly that by modifying the position of the point O_S and O_G in Fig. A.1, different kinds of eccentricities can be set up in this multiphysics model as described in the following:

- Case 1: If O_S doesn't coincide with O and O_G coincides with O_R, it represents the pure input static eccentricity.
- Case 2: If O_S coincides with O and O_G doesn't coincide with O_R, it represents the pure input "dynamic" eccentricity.
- Case 3: If O_S doesn't coincide with O and O_G doesn't coincide with O_R, it represents the input "mix" eccentricity.

Appendix B. Calculation of the maximum permeance coefficient P_{maxc}

$$P_{\mathrm{maxc}} = \begin{cases} \mu_0 \cdot L_m \cdot L_{\mathrm{tr}} & \text{if } 0 \le \tan(\beta) \le \dfrac{|L_{\mathrm{ts}} - L_{\mathrm{tr}}|}{L_m} \\ \mu_0 \cdot \left(\dfrac{L_m \cdot (L_{\mathrm{ts}} + L_{\mathrm{tr}})}{2} - \dfrac{L_m^2 \tan(\beta)}{4} - \dfrac{(L_{\mathrm{ts}} - L_{\mathrm{tr}})^2}{4\tan(\beta)}\right) & \text{if } \dfrac{|L_{\mathrm{ts}} - L_{\mathrm{tr}}|}{L_m} \le \tan(\beta) \le \dfrac{L_{\mathrm{ts}} + L_{\mathrm{tr}}}{L_m} \\ \dfrac{\mu_0 \cdot L_m \cdot L_{\mathrm{tr}}}{\tan(\beta)} & \text{if } \dfrac{L_{\mathrm{ts}} + L_{\mathrm{tr}}}{L_m} \le \tan(\beta) \end{cases} \tag{B.1}$$

where μ_0 is the air permeability, L_m is the core length, L_{ts} and L_{tr} are the effective stator and rotor tooth width respectively and β is the skewed angle of the rotor bar.

Appendix C. Calculation of air-gap permeance variation function $f_p(\theta_{ij})$ and its derivative about the angle $\frac{\mathrm{d}f_p(\theta_{ij})}{\mathrm{d}\theta_{ij}}$

$$f_p(\theta_{ij}) = \begin{cases} 1 & \text{if } -\theta_{ij0} \le \theta_{ij} \le \theta_1 - \theta_{ij0} \text{ and } 2\pi - \theta_1 - \theta_{ij0} \le \theta_{ij} \le 2\pi - \theta_{ij0} \\ \dfrac{1+\cos(\pi\frac{\theta_{ij}-\theta_1}{\theta_2-\theta_1})}{2} & \text{if } \theta_1 - \theta_{ij0} \le \theta_{ij} \le \theta_2 - \theta_{ij0} \\ \dfrac{1+\cos(\pi\frac{\theta_{ij}-2\pi+\theta_1}{\theta_2-\theta_1})}{2} & \text{if } 2\pi - \theta_2 - \theta_{ij0} \le \theta_{ij} \le 2\pi - \theta_1 - \theta_{ij0} \\ 0 & \text{if } \theta_2 - \theta_{ij0} \le \theta_{ij} \le 2\pi - \theta_2 - \theta_{ij0} \end{cases} \tag{C.1}$$

where θ_{ij0} is the initial angular displacement between the defined pair of stator and rotor teeth. Two angle position limits (θ_1, θ_2) are defined in Eq. (C.2) and Eq. (C.3) according to the skewed rotor bars:

$$\theta_1 = \begin{cases} \dfrac{L_{\text{ts}} - L_{\text{tr}} - L_m\tan(\beta)}{D_{\text{ag}}} & \text{if } 0 \le \tan(\beta) \le \dfrac{|L_{\text{ts}} - L_{\text{tr}}|}{L_m} \\ 0 & \text{if } \dfrac{|L_{\text{ts}} - L_{\text{tr}}|}{L_m} \le \tan(\beta) \le \dfrac{L_{\text{ts}} + L_{\text{tr}}}{L_m} \\ \dfrac{L_m\tan(\beta) - L_{\text{ts}} - L_{\text{tr}}}{D_{\text{ag}}} & \text{if } \dfrac{L_{\text{ts}} + L_{\text{tr}}}{L_m} \le \tan(\beta) \end{cases} \tag{C.2}$$

where D_{ag} is the average diameter of stator inner ring and rotor outer ring.

$$\theta_2 = \frac{L_{\text{ts}} + L_{\text{tr}} + O_{\text{ss}} + O_{\text{sr}} + L_m\tan(\beta)}{D_{\text{ag}}} \tag{C.3}$$

with O_{ss} and O_{sr} are respectively the stator and rotor slot open length.

$$\frac{df_p(\theta_{ij})}{d\theta_{ij}} = \begin{cases} 0 & \text{if } -\theta_{ij0} \le \theta_{ij} \le \theta_1 - \theta_{ij0} \text{ and } 2\pi - \theta_1 - \theta_{ij0} \le \theta_{ij} \le 2\pi - \theta_{ij0} \\ -\dfrac{1}{2}\cdot sin(\pi\dfrac{\theta_{ij}-\theta_1}{\theta_2-\theta_1})\cdot\dfrac{\pi}{\theta_2-\theta_1} & \text{if } \theta_1 - \theta_{ij0} \le \theta_{ij} \le \theta_2 - \theta_{ij0} \\ -\dfrac{1}{2}\cdot sin(\pi\dfrac{\theta_{ij}-2\pi+\theta_1}{\theta_2-\theta_1})\cdot\dfrac{\pi}{\theta_2-\theta_1} & \text{if } 2\pi - \theta_2 - \theta_{ij0} \le \theta_{ij} \le 2\pi - \theta_1 - \theta_{ij0} \\ 0 & \text{if } \theta_2 - \theta_{ij0} \le \theta_{ij} \le 2\pi - \theta_2 - \theta_{ij0} \end{cases} \tag{C.4}$$

It is shown in Fig. C.1.

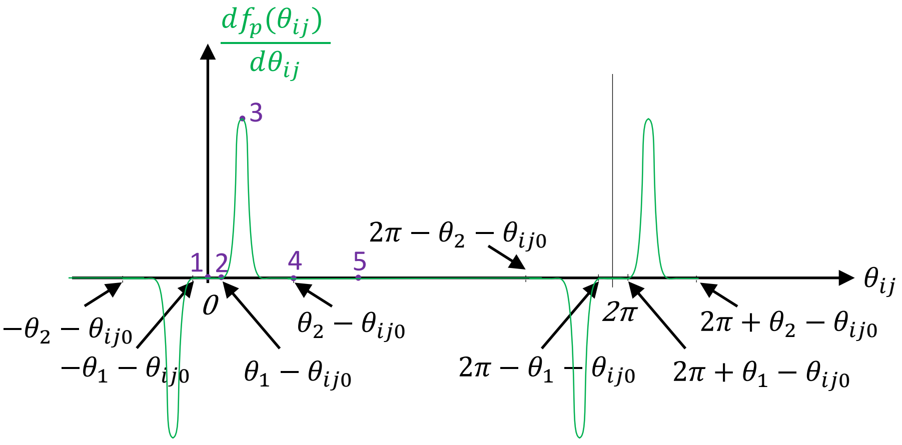

Fig. C.1. Derivative of air-gap permeance between any two teeth versus shaft rotation

Appendix D. Motor parameters and Mechanical model characteristics

Parameter	**Value**
Number of poles	2
Number of phases	3
Number of parallel paths	1
Outer diameter of the stator core [m]	0.2
Inner diameter of the stator core [m]	0.12
Air-gap average length [m]	0.96e-3
Core length [m]	0.165
Number of stator slots	36
Number of rotor slots	30
Effective stator tooth width [m]	0.0075
Effective rotor tooth width [m]	0.0124
Skew of rotor slots [°]	1.34
Connection	Y
Rated voltage [V]	400
Rated frequency [Hz]	50
Rated current [A]	13.5
Rated power [kW]	7.5

Table D.1: Motor parameters

Parameter	**Value**
Mass of the rotor [kg]	17.05
Moment of inertia [kg·m^2]	0.01102
Steel Young's modulus [Gpa]	210
Steel density [kg·m^{-3}]	7800
Steel poisson's ratio	0.3
Shaft length [m]	0.325
Shaft diameter [m]	0.043
Modal damping ratio	0.07
Equivalent bearing stiffness [N·m^{-1}]	5e7

Table D.2: Mechanical model characteristics

References

[1] X. Xu, Q. Han, F. Chu, Review of electromagnetic vibration in electrical machines, Energies 11 (7) (2018) 1779. `doi:10.3390/en11071779`.

URL `https://doi.org/10.3390%2Fen11071779`

[2] A. Arkkio, M. Antila, K. Pokki, A. Simon, E. Lantto, Electromagnetic force on a whirling cage rotor, IEE Proceedings - Electric Power Applications 147 (5) (2000) 353. `doi:10.1049/ip-epa:20000523`.
URL `https://doi.org/10.1049%2Fip-epa%3A20000523`

[3] T. P. Holopainen, A. Tenhunen, A. Arkkio, Electromechanical interaction in rotor vibrations of electric machines, in: Proceedings, 5th World Congress on Computational Mechanics, HA, Mang, FG Rammerstorfer, and J., Eberhardsteiner, eds., Vienna University of Technology, Austria, Vol. 10, 2002.

[4] T. P. Holopainen, A. Tenhunen, A. Arkkio, Electromechanical interaction in rotordynamics of cage induction motors, Vol. 284, Elsevier BV, 2005. `doi:10.1016/j.jsv.2004.07.007`.
URL `https://doi.org/10.1016%2Fj.jsv.2004.07.007`

[5] T. P. Holopainen, A. Tenhunen, E. Lantto, A. Arkkio, Unbalanced magnetic pull induced by arbitrary eccentric motion of cage rotor in transient operation. part 1: Analytical model, Electrical Engineering 88 (1) (2005) 13–24. `doi:10.1007/s00202-004-0257-z`.
URL `https://doi.org/10.1007%2Fs00202-004-0257-z`

[6] M. Donát, Computational modeling of the dynamic behavior of the induction motor rotor, in: I Annals of DAAAM for 2012 & Proceedings of the 23rd International DAAAM Symposium, Vol. 23, 2012, pp. 0191–0194.

[7] M. Donát, D. Dušek, Eccentrically mounted rotor pack and its influence on the vibration and noise of an asynchronous generator, Journal of Sound and Vibration 344 (2015) 503–516. `doi:10.1016/j.jsv.2015.01.033`.
URL `https://doi.org/10.1016%2Fj.jsv.2015.01.033`

[8] R. Belmans, A. Vandenput, W. Geysen, Influence of unbalanced magnetic pull on the radial stability of flexible-shaft induction machines, IEE Proceedings B Electric Power Applications 134 (2) (1987) 101. `doi:10.1049/ip-b.1987.0013`.
URL `https://doi.org/10.1049%2Fip-b.1987.0013`

[9] A. Smith, D. Dorrell, Calculation and measurement of unbalanced magnetic pull in cage induction motors with eccentric rotors. part 1: Analytical model, IEE Proceedings - Electric Power Applications 143 (3) (1996) 193. `doi:10.1049/ip-epa:19960155`.
URL `https://doi.org/10.1049%2Fip-epa%3A19960155`

[10] D. GUO, F. CHU, D. CHEN, THE UNBALANCED MAGNETIC PULL AND ITS EFFECTS ON VIBRATION IN a THREE-PHASE GENERATOR WITH ECCENTRIC ROTOR, Journal of Sound and Vibration 254 (2) (2002) 297–312. `doi:10.1006/jsvi.2001.4088`.
URL `https://doi.org/10.1006%2Fjsvi.2001.4088`

[11] A. D. Gerlando, G. M. Foglia, R. Perini, Analytical modelling of unbalanced magnetic pull in isotropic electrical machines, in: 2008 18th International Conference on Electrical Machines, IEEE, 2008. `doi:10.1109/icelmach.2008.4799998`.
URL `https://doi.org/10.1109%2Ficelmach.2008.4799998`

[12] V. Ostović, Dynamics of Saturated Electric Machines, Springer New York, 1989. `doi:10.1007/978-1-4613-8933-0`.
URL `https://doi.org/10.1007%2F978-1-4613-8933-0`

[13] A. Mahyob, P. Reghem, G. Barakat, Permeance network modeling of the stator winding faults in electrical machines, IEEE Transactions on Magnetics 45 (3) (2009) 1820–1823. `doi:10.1109/tmag.2009.2012780`.
URL `https://doi.org/10.1109%2Ftmag.2009.2012780`

[14] X. Han, A. Palazzolo, Unstable force analysis for induction motor eccentricity, Journal of Sound and Vibration 370 (2016) 230–258. `doi:10.1016/j.jsv.2016.01.045`.
URL `https://doi.org/10.1016%2Fj.jsv.2016.01.045`

[15] H. Kelk, A. Eghbali, H. Toliyat, Modeling and analysis of cage induction motors under rotor misalignment and air gap eccentricity, in: Fourtieth IAS Annual Meeting. Conference Record of the 2005 Industry Applications Conference, 2005., IEEE. `doi:10.1109/ias.2005.1518531`.
URL `https://doi.org/10.1109%2Fias.2005.1518531`

[16] A. Mahyob, M. Y. O. Elmoctar, P. Reghem, G. Barakat, Induction machine modelling using permeance network method for dynamic simulation of air-gap eccentricity, in: 2007 European Conference on Power Electronics and Applications, IEEE, 2007. `doi:10.1109/epe.2007.4417662`.
URL `https://doi.org/10.1109%2Fepe.2007.4417662`

[17] A. Fourati, A. Bourdon, N. Feki, D. Rémond, F. Chaari, M. Haddar, Angular-based modeling of induction motors for monitoring, Journal of Sound and Vibration 395 (2017) 371–392.
URL `https://doi.org/10.1016%2Fj.jsv.2016.12.031`

[18] J. L. Gomez, A. Bourdon, H. André, D. Rémond, Modelling deep groove ball bearing localized defects inducing instantaneous angular speed variations, Tribology International 98 (2016) 270–281. `doi:10.1016/j.triboint.2016.02.032`.
URL `https://doi.org/10.1016%2Fj.triboint.2016.02.032`

[19] M. Babaei, J. Faiz, B. M. Ebrahimi, S. Amini, J. Nazarzadeh, A detailed analytical model of a salient-pole synchronous generator under dynamic eccentricity fault, IEEE Transactions on Magnetics 47 (4) (2011) 764–771. `doi:10.1109/tmag.2011.2105498`.
URL `https://doi.org/10.1109%2Ftmag.2011.2105498`

[20] Y. Zhou, X. Bao, C. Di, L. Wang, Analysis of dynamic unbalanced magnetic pull in induction motor with dynamic eccentricity during starting period, IEEE Transactions on Magnetics 52 (7) (2016) 1–4. `doi:10.1109/tmag.2016.2520950`.
URL `https://doi.org/10.1109%2Ftmag.2016.2520950`

[21] X. Xu, Q. Han, F. Chu, Nonlinear vibration of a generator rotor with unbalanced magnetic pull considering both dynamic and static eccentricities, Archive of Applied Mechanics 86 (8) (2016) 1521–1536. `doi:10.1007/s00419-016-1133-9`.
URL `https://doi.org/10.1007%2Fs00419-016-1133-9`

[22] C. Delforge, B. Lemaire-Semail, Induction machine modeling using finite element and permeance network methods, IEEE Transactions on Magnetics 31 (3) (1995) 2092–2095. `doi:10.1109/20.376457`.
URL `https://doi.org/10.1109%2F20.376457`

[23] P. Pennacchi, Computational model for calculating the dynamical behaviour of generators caused by unbalanced magnetic pull and experimental validation, Journal of Sound and Vibration 312 (1-2) (2008) 332–353. `doi:10.1016/j.jsv.2007.10.052`.
URL `https://doi.org/10.1016%2Fj.jsv.2007.10.052`

[24] D. Meeker, Finite Element Method Magnetics User's Manual Version 4.2 (2020).
URL `http://www.femm.info/wiki/Documentation/`

[25] A. Tenhunen, T. Holopainen, A. Arkkio, Effects of equalizing currents on electromagnetic forces of whirling cage rotor, in: IEEE International Electric Machines and Drives Conference, 2003. IEMDC'03., IEEE. `doi:10.1109/iemdc.2003.1211272`.
URL `https://doi.org/10.1109%2Fiemdc.2003.1211272`

[26] R. Belmans, A. Vandenput, W. Geysen, Calculation of the flux density and the unbalanced pull in two pole induction machines, Archiv für Elektrotechnik 70 (3) (1987) 151–161. `doi:10.1007/bf01574064`.
URL `https://doi.org/10.1007%2Fbf01574064`